



Multi-material topology optimization for maximizing structural stability under thermo-mechanical loading

Wang, Yafeng; Sigmund, Ole

Published in:
Computer Methods in Applied Mechanics and Engineering

Link to article, DOI:
[10.1016/j.cma.2023.115938](https://doi.org/10.1016/j.cma.2023.115938)

Publication date:
2023

Document Version
Publisher's PDF, also known as Version of record

[Link back to DTU Orbit](#)

Citation (APA):
Wang, Y., & Sigmund, O. (2023). Multi-material topology optimization for maximizing structural stability under thermo-mechanical loading. *Computer Methods in Applied Mechanics and Engineering*, 407, Article 115938. <https://doi.org/10.1016/j.cma.2023.115938>

General rights

Copyright and moral rights for the publications made accessible in the public portal are retained by the authors and/or other copyright owners and it is a condition of accessing publications that users recognise and abide by the legal requirements associated with these rights.

- Users may download and print one copy of any publication from the public portal for the purpose of private study or research.
- You may not further distribute the material or use it for any profit-making activity or commercial gain
- You may freely distribute the URL identifying the publication in the public portal

If you believe that this document breaches copyright please contact us providing details, and we will remove access to the work immediately and investigate your claim.



Multi-material topology optimization for maximizing structural stability under thermo-mechanical loading

Yafeng Wang^{*}, Ole Sigmund

Department of Civil and Mechanical Engineering, Technical University of Denmark, Koppels Alle 404, 2800 Kongens Lyngby, Denmark

Received 24 October 2022; received in revised form 10 January 2023; accepted 1 February 2023

Available online xxxx

Abstract

Mechanical structures are often simultaneously subjected to thermal and mechanical loading, both of which can lead to buckling failure. Developing efficient structural forms with better capacity for stability is important to keep structures safe. This study aims to optimize structural buckling capacity by using a density-based topology optimization scheme. Instead of treating the mechanical and thermal loadings as a single coupled part in the linearized buckling analysis, the effects of mechanical and thermal loadings are decoupled, which allows to separately analyze and optimize buckling aspects induced by mechanical or thermal loading. Two optimization models based on the decoupled analysis models are developed to respectively maximize the critical load factor of buckling induced by mechanical loading under a specified thermal loading and buckling induced by thermal loading under a specified mechanical loading. Further, based on a three-phase material model, a multi-material topology optimization scheme is employed to optimize the buckling capacity of active structures made of structural and actuating materials and prestressed structures containing prestressed components. The actuation effects are mimicked by the thermal loading of active material. The sensitivities of the objective functions and constraints are derived through the adjoint technique, and the method of moving asymptotes (MMA) is employed to solve the topology optimization problems. Numerical examples are adopted to verify the effectiveness of the proposed approach.

© 2023 The Author(s). Published by Elsevier B.V. This is an open access article under the CC BY license (<http://creativecommons.org/licenses/by/4.0/>).

Keywords: Multi-material; Topology optimization; Stability; Buckling; Thermo-mechanical loading; Active/prestressed structure

1. Introduction

Structural topology optimization has been developed for decades and has drawn more and more attention in the research and industry fields [1–4]. Several approaches, such as homogenization [5], solid isotropic material with penalization (SIMP) [6], evolutionary structural optimization (ESO) [7], level set method [8], moving morphable components (MMC) [9] have been proposed to efficiently carry out the topology optimization on a range of problems. Optimal structural design covers a variety of physical problems, such as optimizing structural stiffness [10], strength [11], and stability [12]. Among these problems, optimal design with respect to stability or buckling is a rather important but challenging issue that has been thoroughly studied [12–15].

Structural design considering buckling criteria dates back decades when it mainly dealt with the design of trusses, where stability was imposed on the local level, constraining the maximum stress or displacement of individual

^{*} Corresponding author.

E-mail addresses: yafwa@dtu.dk (Y. Wang), olsi@dtu.dk (O. Sigmund).

members [12,16]. Then, several methods have been proposed to consider overall structural stability [13,17,18]. For continuum structures, Neves et al. [19] firstly investigated the maximization of the linearized buckling load based on a homogenization-based topology optimization method. Folgado and Rodrigues [20] studied the reinforcement problem for a plate considering buckling criterion. Due to the specific and often counter-acting character of buckling design, as opposed to compliance or stress designs, it is apparent that the former must be carefully treated in the optimization, especially for complex structures. Therefore, a renewed interest in topology design with regard to buckling is rising.

Recently, Gao et al. [21–23] re-studied buckling-based topology optimization that focused on alleviating the issues due to pseudo buckling modes and the conflict between the requirements for structural stiffness and stability. Lindgaard et al. [24] studied buckling-based topology optimization considering geometrically nonlinearity. Dunning et al. [25] and Bian and Feng [26] proposed to use effective iterative methods for solving the large eigenvalue problem in large-scale buckling-constrained topology optimization problems. Cheng and Xu [27] optimized the topologies of stiffened plates and material microstructures considering buckling criteria. Thomsen et al. [28] carried out the design of periodic microstructures with respect to multi-scale buckling conditions. Ye et al. [29] and Wang et al. [30] investigated the topological optimization of plate/shell and lightweight structures subjected to linear buckling constraints and frequency constraints based on the Independent Continuous Mapping Method (ICM) [31]. Ferrari and Sigmund [32] revisited topology optimization with buckling constraints and gave a comprehensive discussion on several important issues in buckling-constrained topology optimization, such as the competition between stiffness and stability requirements, the activation of several buckling modes, the use of non-conforming finite elements for the analysis, and the use of inconsistent sensitivity. Further, a 250-line Matlab code was provided by Ferrari et al. [33] for topology optimization for linearized buckling criteria, which uses efficient strategies to significantly cut the computational bottlenecks in linearized buckling topology optimization.

The works mentioned above all deal with buckling induced by pure mechanical loading. In practical scenarios, thermal loading may also lead to buckling failure since a temperature rise may cause severe compression in the structure. Therefore, the effect of thermal loading or coupled thermo-mechanical loading on the buckling capacity should also be considered for optimal structural design. In this regard, Singha et al. [34] and Malekzadeh et al. [35] adopted a genetic algorithm (GA) to optimize the fiber orientation and thickness of laminated composites to maximize the buckling load induced by thermal effects. Kamarian et al. [36] optimized the stacking sequence of laminated structures to enhance the buckling temperature. Apart from buckling induced only by thermal loading, the buckling-based structural optimization under thermo-mechanical loading is also investigated by some. For example, Deng et al. [37] used a level-set approach to solve a buckling-constrained problem under thermo-mechanical loading for a single material case. Stanford and Beran [38] employed the SIMP approach to develop a buckling-constrained topology optimization framework of a metallic panel structure subjected to thermo-mechanical loading. Recently, Wu et al. [39] adopted the rational approximation of material properties (RAMP) [40] interpolation scheme to address the multi-material topology optimization problems considering thermo-mechanical loading to enhance the structural buckling resistance capacity. Gan and Wang used the SIMP approach to explore the size effect under thermal buckling criterion [41] and considered the influence of the thermo-solid coupling field on the buckling performance of porous infill structures [42]. Lee et al. [43] proposed a topography optimization method and a size optimization method to control linear buckling temperature and thermal buckling modes of composite plate structures.

In all the studies mentioned above on the buckling under thermo-mechanical loading, the thermal load and mechanical load are formulated as a single coupled part to compute the stress/geometrical stiffness matrix in the linearized buckling analysis, i.e., the thermal load and mechanical load are scaled simultaneously by the same buckling load factor in the eigenvalue analysis. This kind of formulation implies that thermal load and mechanical load are not independent and always proportional to each other. This is a very strong assumption from a practical point of view because thermal load and mechanical load are usually independent of each other, and buckling can be caused by either of them separately. To be able to separately investigate the thermal load and mechanical load on the buckling, it is better to decouple the effects of the two types of loads in the buckling analysis, which allows one to separately analyze the buckling induced by mechanical or thermal loading. Based on the decoupled formulations, two optimization models are developed in this study to respectively maximize the critical load factor of buckling induced by mechanical loading under a specified thermal loading and the buckling induced by thermal loading under a specified mechanical loading.

In the topology optimization field, thermal expansion effects have been employed to mimic the actuation property of a material. For example, Sigmund [44,45] proposed a topology optimization method to design multiphysics actuators and electro-thermo-mechanical systems based on material thermal expansion effects through a one-material or two-material scheme. Jensen et al. [46] proposed a systematic topology optimization approach for simultaneously designing the morphing functionality and actuation in three-dimensional wing structures in which the actuation was modeled by a thermal-like linear-strain-based expansion in the actuation material. Based on the decoupled formulations developed in this study and utilizing the thermal expansion effect, a three-phase multi-material topology optimization scheme [45] is further adopted to optimize the buckling capacity of active structures that are made of structural and actuating materials and prestressed structures that contain prestress in the structural members. It shows that, compared to topology-optimized passive structures, stability can be considerably improved for topology-optimized active and prestressed structures.

The outline of the paper is as follows: Section 2 introduces basic formulations for the decoupled models for linearized buckling analysis under thermo-mechanical loading; Section 3 develops the single-material topology optimization model for the maximization of buckling capacity of single-material structures and the multiple-material topology optimization model for the maximization of buckling capacity of active and prestressed structures; Section 4 presents numerical examples to verify the effectiveness of the proposed approach; finally, Section 5 discusses and concludes the paper.

2. Basic formulations for thermo-mechanical buckling analysis

2.1. Linearized buckling analysis under mechanical loading

Considering a discretized mechanical system under only mechanical loading \mathbf{P}_m , the linearized buckling analysis [47] can be done by solving the following eigenvalue problem

$$[\mathbf{K} + \lambda \mathbf{G}_m] \boldsymbol{\varphi} = \mathbf{0}, \quad \boldsymbol{\varphi} \neq \mathbf{0} \quad (1)$$

where \mathbf{K} is the linear, symmetric, and positive definite stiffness matrix, \mathbf{G}_m is the stress/geometric stiffness matrix caused by the mechanical loading and can be assembled from the element stresses. The stress vector $\boldsymbol{\sigma}_{m,e}$ for each element can be calculated by

$$\boldsymbol{\sigma}_{m,e} = \mathbf{D}_e \boldsymbol{\varepsilon}_{m,e} = \mathbf{D}_e \mathbf{B}_e \mathbf{U}_{m,e} \quad (2)$$

where \mathbf{D}_e , \mathbf{B}_e , and $\mathbf{U}_{m,e}$ are the constitutive matrix, strain–displacement matrix, and displacement vector of element e , respectively. The equilibrium displacement \mathbf{U}_m is computed by

$$\mathbf{K} \mathbf{U}_m = \mathbf{P}_m \quad (3)$$

λ and $\boldsymbol{\varphi}$ are respectively the critical buckling load factor (BLF) and the associated buckling mode. In practical buckling analysis, the fundamental BLF λ_1 , associated with the critical load $\mathbf{P}_{cr} = \lambda_1 \mathbf{P}_m$, is what determines the stability of the structure.

2.2. Linearized buckling analysis under thermo-mechanical loading

Following a similar formula as in Eq. (1), the linearized buckling analysis under thermo-mechanical loading may be realized by solving the following eigenvalue problem

$$[\mathbf{K} + \lambda \mathbf{G}] \boldsymbol{\varphi} = \mathbf{0}, \quad \boldsymbol{\varphi} \neq \mathbf{0} \quad (4)$$

where in this case \mathbf{G} is the stress/geometric stiffness matrix caused by the combined effect of thermal and mechanical loadings, i.e., $\mathbf{G} = \mathbf{G}_t + \mathbf{G}_m$. Here, \mathbf{G}_m depends on the mechanical load as outlined in Section 2.1 and \mathbf{G}_t can be assembled from the element stresses caused by thermal loading that is given by

$$\boldsymbol{\sigma}_{t,e} = \mathbf{D}_e (\boldsymbol{\varepsilon}_{t,e} - \boldsymbol{\varepsilon}_{\Delta T,e}) = \mathbf{D}_e (\mathbf{B}_e \mathbf{U}_{t,e} - \alpha_e \boldsymbol{\Phi}^T \Delta T_e) \quad (5)$$

where α_e and ΔT_e are respectively the thermal expansion coefficient and temperature variation of element e , $\mathbf{U}_{t,e}$ is the displacement of element e caused by thermal loading, and $\boldsymbol{\Phi} = [1 \ 1 \ 0]^T$ is a constant vector for two-dimensional problems. The equilibrium displacement \mathbf{U}_t under thermal loading \mathbf{P}_t is solved by

$$\mathbf{K} \mathbf{U}_t = \mathbf{P}_t \quad (6)$$

where \mathbf{P}_t is the thermal loading vector given by

$$\mathbf{P}_t = \sum_e \int_{V_e} \mathbf{B}_e^T \mathbf{D}_e \boldsymbol{\varepsilon}_{\Delta T, e} dV \tag{7}$$

where V_e is the volume of element e .

Eq. (4) can be re-expressed as

$$[\mathbf{K} + \lambda (\mathbf{G}_t + \mathbf{G}_m)] \boldsymbol{\varphi} = \mathbf{0}, \quad \boldsymbol{\varphi} \neq \mathbf{0} \tag{8}$$

By solving this eigenvalue problem, the critical load \mathbf{P}_{cr} is then given by $\mathbf{P}_{cr} = \lambda_1 (\mathbf{P}_t + \mathbf{P}_m)$.

The formulation presented above has been widely adopted for the linearized buckling analysis and buckling-related topology optimization under thermo-mechanical loading [37–39,41,42]. However, in the above formulation, the BLF λ scales \mathbf{G}_t and \mathbf{G}_m simultaneously, which implies that thermal loading \mathbf{P}_t and mechanical loading \mathbf{P}_m are always proportional to each other. This is a strong assumption that is seldom satisfied in practice because in most instances thermal loading and mechanical loading are independent of each other. Therefore, the above formulation may not be able to lead to reasonable results in terms of critical buckling load.

A more reasonable way is to decouple the effects of thermal and mechanical loading in the buckling analysis, i.e., the BLF λ scales \mathbf{G}_t or \mathbf{G}_m respectively instead of scaling them simultaneously. In this way, we can obtain two decoupled formulations as follows

$$[\mathbf{K} + \mathbf{G}_t + \lambda \mathbf{G}_m] \boldsymbol{\varphi} = \mathbf{0}, \quad \boldsymbol{\varphi} \neq \mathbf{0} \tag{9}$$

$$[\mathbf{K} + \mathbf{G}_m + \lambda \mathbf{G}_t] \boldsymbol{\varphi} = \mathbf{0}, \quad \boldsymbol{\varphi} \neq \mathbf{0} \tag{10}$$

Solving the eigenvalue problem in Eq. (9) allows us to analyze the buckling induced by mechanical loading under a specified thermal loading while solving the eigenvalue problem in Eq. (10) allows analyzing the buckling induced by thermal loading under a specified mechanical loading. For brevity, Eqs. (9) and (10) can be rewritten into compact forms as

$$[\mathbf{K}' + \lambda \mathbf{G}_m] \boldsymbol{\varphi} = \mathbf{0}, \quad \boldsymbol{\varphi} \neq \mathbf{0} \tag{11}$$

$$[\mathbf{K}'' + \lambda \mathbf{G}_t] \boldsymbol{\varphi} = \mathbf{0}, \quad \boldsymbol{\varphi} \neq \mathbf{0} \tag{12}$$

where $\mathbf{K}' = \mathbf{K} + \mathbf{G}_t$ and $\mathbf{K}'' = \mathbf{K} + \mathbf{G}_m$. In the following, the original model Eq. (4), and decoupled models Eqs. (11) and (12) are referred to as model #1, model #2, and model #3, respectively.

Next, let us adopt a simple example shown in Fig. 1(a) to compare the difference between using different models for linearized buckling analysis. The two ends of the bar are pin-supported and a horizontal mechanical load is applied to the center of the bar; meanwhile, a temperature variation ΔT gives a uniformly distributed thermal load inside the bar. Eqs. (4) and (11) are respectively employed to perform the buckling analysis.

Fig. 1(b) shows the comparison of the fundamental BLF λ_1 obtained by using model #1 and model #2 under different ΔT . As can be seen, with the increase of ΔT , fundamental BLFs obtained by the two models both decrease because positive ΔT will induce compression in the bar (reduces the buckling resistance capacity). However, the trends of the two curves are different: the curve of model #1 is upward concave while that of model #2 is downward concave; this results in the fundamental BLF obtained through model #2 approaching zero at a certain ΔT , which means that the bar already buckles under the current thermal load even if no mechanical loading exists. This is consistent with the actual situation in practice. In contrast, the curve of model #1 tends to never be zero; this is because the effects of thermal loading and mechanical loading are scaled by λ_1 simultaneously, hence once λ_1 decreases the effects of \mathbf{G}_t and \mathbf{G}_m also decrease, which makes λ_1 never reach zero. On the other hand, it can be seen that the two curves coincide at two points: one is for $\Delta T = 0$ and the other one is for $\lambda_1 = 1$, in which cases the formulas of model #1 and model #2 are identical.

A similar analysis can be carried out to compare model #1 and model #3 based on the fundamental BLF λ_1 under different mechanical loading P (Fig. 1(c)). Note that the curves in (Fig. 1(c)) are symmetrical with respect to the vertical axis due to the symmetry of the bar. From the analysis and comparisons above, it can be concluded that the decoupled models have a clearer and more practical physical meaning for linearized buckling analysis. Therefore, the two decoupled models will be adopted in the following to analyze buckling induced by mechanical loading under a specified thermal loading and buckling induced by thermal loading under a specified mechanical loading.

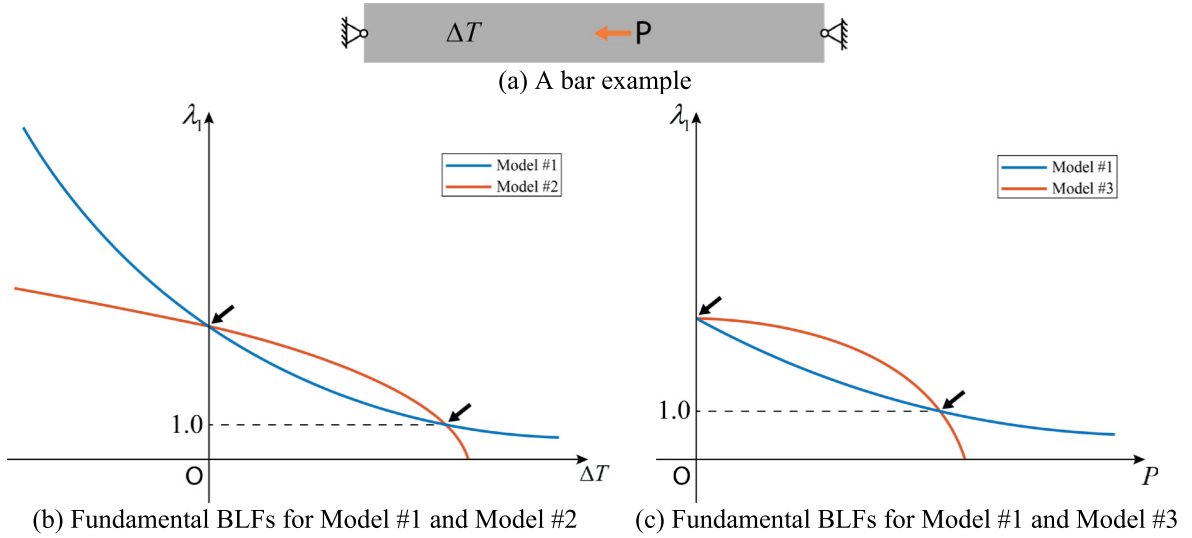


Fig. 1. Comparison of fundamental buckling load factors obtained by different models.

3. Thermo-mechanical buckling topology optimization

3.1. Single-material topology optimization model

The density-based topology optimization approach [6] is employed in this study to maximize the fundamental BLF. For a regular finite element mesh, the design variables are defined as the relative densities of the elements, i.e., $\mathbf{x} = \{x_e\}$. In order to avoid mesh dependency and checkerboard patterns [6] and enhance the discreteness of the designs, a three-field approach [48] is employed. The elementwise density fields are first filtered by using the density filter

$$\bar{x}_e = \frac{1}{\sum_{i \in N_e} H_{ei}} \sum_{i \in N_e} H_{ei} x_i \tag{13}$$

where \bar{x}_e is the filtered design variables, N_e is the set of element i for which the center-to-center distance $\Delta(e, i)$ to element e is smaller than the filter radius r_{min} , and is the typical linear distance function

$$H_{ei} = \max(0, r_{min} - \Delta(e, i)) \tag{14}$$

Physical density fields are then obtained by a modified smooth Heaviside function

$$\tilde{x}_e = \frac{\tanh(\beta\theta) + \tanh(\beta(\bar{x}_e - \theta))}{\tanh(\beta\theta) + \tanh(\beta(1 - \theta))} \tag{15}$$

where β controls the steepness/sharpness of the function and θ sets the threshold value.

The design-dependent stiffness matrices \mathbf{K} , \mathbf{G}_t , and \mathbf{G}_m are assembled from the element ones, i.e., $\mathbf{k}_e(\tilde{x}_e)$, $\mathbf{g}_{e,t}(\tilde{x}_e, \mathbf{U}_{t,e})$, and $\mathbf{g}_{e,m}(\tilde{x}_e, \mathbf{U}_{m,e})$, which are parameterized by interpolation functions as

$$\begin{aligned} \mathbf{k}_e(\tilde{x}_e) &= h_1(\tilde{x}_e) \mathbf{k}_0 \\ \mathbf{g}_{e,t}(\tilde{x}_e, \mathbf{U}_{t,e}) &= h_2(\tilde{x}_e) \mathbf{g}_0(\mathbf{U}_{t,e}) \\ \mathbf{g}_{e,m}(\tilde{x}_e, \mathbf{U}_{m,e}) &= h_2(\tilde{x}_e) \mathbf{g}_0(\mathbf{U}_{m,e}) \end{aligned} \tag{16}$$

where local matrices \mathbf{k}_0 , $\mathbf{g}_0(\mathbf{U}_{t,e})$, and $\mathbf{g}_0(\mathbf{U}_{m,e})$ correspond to unit elastic modulus and are independent of \tilde{x}_e . The local stress stiffness matrix $\mathbf{g}_0(\mathbf{U}_{m,e})$ can be computed by [49]

$$\mathbf{g}_0(\mathbf{U}_{m,e}) = \int_{V_e} \mathbf{B}^T \mathbf{S}_{m,e}^0 \mathbf{B} dV \tag{17}$$

where \mathbf{B} discretizes the deformation gradient and for a Q_4 bilinear element reads [50]

$$\mathbf{B} = \begin{bmatrix} \partial_x N_1 & 0 & \partial_x N_2 & 0 & \partial_x N_3 & 0 & \partial_x N_4 & 0 \\ \partial_y N_1 & 0 & \partial_y N_2 & 0 & \partial_y N_3 & 0 & \partial_y N_4 & 0 \\ 0 & \partial_x N_1 & 0 & \partial_x N_2 & 0 & \partial_x N_3 & 0 & \partial_x N_4 \\ 0 & \partial_y N_1 & 0 & \partial_y N_2 & 0 & \partial_y N_3 & 0 & \partial_y N_4 \end{bmatrix} \quad (18)$$

$\mathbf{S}_{m,e}^0 = \mathbf{I} \otimes \hat{\boldsymbol{\sigma}}_{m,e}^0$ with $\hat{\boldsymbol{\sigma}}_{m,e}^0 = \hat{\boldsymbol{\sigma}}_{m,e}^0(\mathbf{U}_{m,e})$ being the element stress tensor corresponding to unit elastic modulus. The local stress stiffness matrix $\mathbf{g}_0(\mathbf{U}_{t,e})$ can be computed in a similar way. For more details and implementation of the element stress stiffness matrix, we refer the reader to [50].

The interpolations in Eq. (16) can be realized by defining the constitutive matrix \mathbf{D}_e in Eqs. (2) and (5) as

$$\mathbf{D}_e = \begin{cases} h_1(\tilde{x}_e) \mathbf{D}_0, & \text{for the assembly of } \mathbf{K} \\ h_2(\tilde{x}_e) \mathbf{D}_0, & \text{for the assembly of } \mathbf{G}_t \text{ and } \mathbf{G}_m \end{cases} \quad (19)$$

where \mathbf{D}_0 is the constitutive matrix with unit elastic modulus.

Considering an isotropic base material, in the following we use

$$\begin{aligned} h_1(\tilde{x}_e) &= E_{\min} + \tilde{x}_e^p (E - E_{\min}) \\ h_2(\tilde{x}_e) &= \tilde{x}_e^p E \end{aligned} \quad (20)$$

where E and E_{\min} are respectively Young’s modulus of the solid and void, and p is the penalization factor. The interpolation schemes in Eq. (20) have been proven to be an effective choice against pseudo-buckling modes, at least for the material contrast of interest ($E/E_{\min} = 10^6$) used in this study [21,32].

Next, we consider a topology optimization problem to maximize the fundamental BLF under compliance and material volume constraints, which is expressed as

$$\begin{cases} \max_{\mathbf{x}} \lambda_{\min} \\ \text{s.t. } V(\tilde{\mathbf{x}}) \leq \bar{V} \\ C(\tilde{\mathbf{x}}) \leq \bar{C} \end{cases} \quad (21)$$

where λ_{\min} is the fundamental BLF given by $\lambda_{\min} = \min_{i \in \Theta} \lambda_i$ in which Θ is a subset of all the eigenvalues that are considered in the optimization; $V(\tilde{\mathbf{x}})$ and $C(\tilde{\mathbf{x}})$ are the volume and compliance of the structure while \bar{V} and \bar{C} are the corresponding upper bounds. Notably, this study only focuses on the effect of thermal loading on buckling. Considering the compliance measure, we treat it in the original mechanical sense: as the work of external mechanical forces is independent of the thermal loads. In this way, we ensure mechanical meaning and avoid issues with negative compliances associated with other difficulties, c.f. [51].

Taking model #2 as an example, from a computational point of view, it is more convenient to transform the eigenvalue equation Eq. (11) into

$$[\mu \mathbf{K}' + \mathbf{G}_m] \boldsymbol{\varphi} = \mathbf{0}, \quad \boldsymbol{\varphi} \neq \mathbf{0} \quad (22)$$

with the relationship $\lambda = 1/\mu$, such that the fundamental BLF λ_1 is associated with the maximum algebraic value of μ , say μ_1 that can be approximated by using the Kreisselmeier–Steinhauser (K-S) aggregation function [52] by

$$J^{KS}[\mu_i] = \mu_1 + \frac{1}{q} \ln \left(\sum_{i \in \Theta} e^{q(\mu_i - \mu_1)} \right) \quad (23)$$

where q is the aggregation parameter.

From the analysis in Section 2.2, the fundamental BLF obtained through model #2 will approach zero (i.e., $\lambda = 0$) at a certain ΔT , which means that the bar already buckles under the associating thermal load even if no mechanical loading exists. In this case, the governing equation Eq. (11) reduces to

$$[\mathbf{K} + \mathbf{G}_t] \boldsymbol{\varphi} = \mathbf{0}, \quad \boldsymbol{\varphi} \neq \mathbf{0} \quad (24)$$

which is equivalent to the condition that the following eigenvalue problem has a minimum eigenvalue of $\omega = 1$

$$[\mathbf{K} + \omega \mathbf{G}_t] \boldsymbol{\varphi} = \mathbf{0}, \quad \boldsymbol{\varphi} \neq \mathbf{0} \quad (25)$$

In practice, it should be required that the structure will not buckle under the thermal loading (i.e., under the effect of \mathbf{G}_t) alone, therefore, the fundamental eigenvalue of Eq. (25) should be larger than 1.0. In the optimization, a lower bound $\underline{\omega}$ that is a bit larger than 1.0 can be assigned to enforce a scaling factor for ω_1 , i.e., $\omega_{\min} \geq \underline{\omega}$. Similar to Eq. (22), Eq. (25) can be transformed into

$$[\gamma \mathbf{K} + \mathbf{G}_t] \boldsymbol{\varphi} = \mathbf{0}, \quad \boldsymbol{\varphi} \neq \mathbf{0} \tag{26}$$

where $\omega = 1/\gamma$. Then γ_1 can be approximated by using the K-S aggregation function by

$$J^{KS} [\gamma_i] = \gamma_1 + \frac{1}{q} \ln \left(\sum_{i \in \Theta} e^{q(\gamma_i - \gamma_1)} \right) \tag{27}$$

Based on Eqs. (26) and (27), the additional constraint $\omega_{\min} \geq \underline{\omega}$ can be re-expressed as

$$J^{KS} [\gamma_i] \leq \frac{1}{\underline{\omega}} \tag{28}$$

Then, the final optimization model can be written as

$$\begin{cases} \min_{\mathbf{x}} J^{KS} [\mu_i] \\ \text{s.t. } g_V = V(\tilde{\mathbf{x}}) / \bar{V} - 1 \leq 0 \\ \quad g_C = C(\tilde{\mathbf{x}}) / \bar{C} - 1 \leq 0 \\ \quad g_B = \underline{\omega} J^{KS} [\gamma_i] - 1 \leq 0 \end{cases} \tag{29}$$

The established topology optimization model also applies to model #3 to maximize the fundamental buckling load for thermal loading under a specified mechanical loading, with Eq. (11) exchanged by Eq. (12).

3.2. Multi-material topology optimization model

To carry out multi-material topology optimization problems, more design variables should be introduced for each element to determine its material phase. A two-material topology optimization model is considered in this study but the concept can be extended to cases with more than two materials. Two design variables per element are introduced to parameterize the material distribution, i.e., a material density design variable ξ_e and a material phase design variable η_e with $\xi_e, \eta_e \in [0, 1]$. Hence, the design variable vector is

$$\mathbf{x} = \{\boldsymbol{\xi}, \boldsymbol{\eta}\}^T \tag{30}$$

Then filter and projection as presented in Section 3.1 are also applied to $\boldsymbol{\xi}$ and $\boldsymbol{\eta}$ to get the physical-field variables $\tilde{\mathbf{x}} = \{\tilde{\boldsymbol{\xi}}, \tilde{\boldsymbol{\eta}}\}^T$. Based on a three-phase material model, $\tilde{\xi}_e = 1$ and $\tilde{\eta}_e = 1$ indicate that the element is occupied by active material, $\tilde{\xi}_e = 1$ and $\tilde{\eta}_e = 0$ by passive material, and $\tilde{\xi}_e = 0$ by void. Hence, the volumes of the active and passive materials are calculated by

$$V_a = \sum_e V_e \tilde{\xi}_e \tilde{\eta}_e, \quad V_p = \sum_e V_e \tilde{\xi}_e (1 - \tilde{\eta}_e) \tag{31}$$

Then the volume of the entire structure is given by $V = V_a + V_p$.

The three-phase material model proposed by Sigmund [45] to interpolate the elemental material properties (shear modulus G , bulk module K , and thermal expansion coefficient α) is employed, given as

$$\begin{aligned} G(\tilde{\xi}_e, \tilde{\eta}_e) &= \tilde{\xi}_e^p \Phi_G(\tilde{\eta}_e) \\ K(\tilde{\xi}_e, \tilde{\eta}_e) &= \tilde{\xi}_e^p \Phi_K(\tilde{\eta}_e) \\ \alpha(\tilde{\eta}_e) &= \frac{(K_1 \alpha_1 - K_2 \alpha_2) K(\tilde{\eta}_e) - K_1 K_2 (\alpha_1 - \alpha_2)}{K(\tilde{\eta}_e) (K_1 - K_2)} \end{aligned} \tag{32}$$

where K_1 and K_2 are respectively the bulk moduli of materials 1 and 2, α_1 and α_2 are respectively the thermal expansion coefficients of materials 1 and 2, the phase interpolation $\Phi_G(\tilde{\eta}_e)$ and $\Phi_K(\tilde{\eta}_e)$ are defined as

$$\begin{aligned} \Phi_G(\tilde{\eta}_e) &= (1 - \Psi) G_L^{HSW}(\tilde{\eta}_e) + \Psi G_U^{HSW}(\tilde{\eta}_e) \\ \Phi_K(\tilde{\eta}_e) &= (1 - \Psi) K_L^{HS}(\tilde{\eta}_e) + \Psi K_U^{HS}(\tilde{\eta}_e) \end{aligned} \tag{33}$$

In the above formulations, G_L^{HSW} and G_U^{HSW} are the lower and upper Hashin–Shtrikman–Walpole (HSW) bounds on the shear modulus, and K_L^{HS} and K_U^{HS} are the lower and upper Hashin–Shtrikman (HS) bounds on the bulk modulus. Their exact formulas depend on the property values (shear and bulk modulus) of the two materials (for more details about the exact formulas the reader is referred to [45]). $\Psi \in [0, 1]$ interpolates linearly between the lower and upper bounds and works as a penalization mechanism for intermediate densities, and $\Psi = 1$ is adopted in this study. $K(\tilde{\eta}_e)$ is found from Eq. (32) by setting $\tilde{\xi}_e = 1$. Note that by using the three-phase material interpolation functions, all the physical parameters can be ensured to be within the physically realizable bounds for any densities [45].

For two-dimensional plane stress problems, the interpolation for Young’s modulus is expressed as

$$h(\tilde{\xi}_e, \tilde{\eta}_e) = \frac{4K(\tilde{\xi}_e, \tilde{\eta}_e)G(\tilde{\xi}_e, \tilde{\eta}_e)}{K(\tilde{\xi}_e, \tilde{\eta}_e) + G(\tilde{\xi}_e, \tilde{\eta}_e)} \tag{34}$$

Then following a similar analysis procedure as stated in Section 3.1, the topology optimization model considering two materials can be formulated as follows

$$\begin{cases} \min_{\mathbf{x}} J^{KS}[\mu_i] \\ \text{s.t. } g_V = V(\tilde{\mathbf{x}})/\bar{V} - 1 \leq 0 \\ \quad g_C = C(\tilde{\mathbf{x}})/\bar{C} - 1 \leq 0 \\ \quad g_B = \omega J^{KS}[\gamma_i] - 1 \leq 0 \\ \quad g_{V_a} = V_a(\tilde{\mathbf{x}})/\bar{V}_a - 1 \leq 0 \end{cases} \tag{35}$$

Note that an additional constraint to assign an upper bound to the active material volume occupation is considered in Eq. (35) for completeness.

3.3. Sensitivity analysis

The adjoint method [6] is employed to calculate the sensitivities of a function f (objective function or constraint function). The sensitivities of f with respect to the physical-field variable \tilde{x}_e is obtained through

$$\frac{\partial f}{\partial \tilde{x}_e} = \frac{\partial f}{\partial \tilde{x}_e} + \boldsymbol{\chi}_m^T \left(\frac{\partial \mathbf{K}}{\partial \tilde{x}_e} \mathbf{U}_m + \mathbf{K} \frac{\partial \mathbf{U}_m}{\partial \tilde{x}_e} - \frac{\partial \mathbf{P}_m}{\partial \tilde{x}_e} \right) + \boldsymbol{\chi}_t^T \left(\frac{\partial \mathbf{K}}{\partial \tilde{x}_e} \mathbf{U}_t + \mathbf{K} \frac{\partial \mathbf{U}_t}{\partial \tilde{x}_e} - \frac{\partial \mathbf{P}_t}{\partial \tilde{x}_e} \right) \tag{36}$$

where $\boldsymbol{\chi}_m$ and $\boldsymbol{\chi}_t$ are the adjoint vectors. Detailed derivations are given in Appendix. Then the sensitivities of f with respect to the design variable x_e are calculated by using the chain rule

$$\frac{\partial f}{\partial x_e} = \sum_i \frac{\partial f}{\partial \tilde{x}_i} \frac{\partial \tilde{x}_i}{\partial x_i} \frac{\partial x_i}{\partial x_e} \tag{37}$$

3.4. On undesirable parasitic mode phenomenon

The undesirable parasitic mode phenomenon may happen in the SIMP and other fictitious density approaches for the topology optimization considering design-dependent loads (e.g., self-weight load and thermal stress load) [53,54]; the reason is that different exponents are adopted for the power-law interpolations of elastic modulus and material density (for self-weight load cases)/thermal expansion coefficient (for thermal stress load cases), which may make the elements with extremely low densities have relatively small stiffness to support the self-weight load or thermal stress load [53,54]. To address this issue, modified interpolation laws were proposed for elastic modulus to limit the ratio between the self-weight load and the stiffness to a given finite value for low-density elements [53,55]. Also, it was verified that the RAMP model [40], which is smooth everywhere and always has a positive (non-zero) slope at zero density, can be employed to avoid the undesirable parasitic phenomenon [54].

In this study, the SIMP model is adopted and only the elastic modulus is penalized (the thermal expansion coefficient is not penalized) for the single-material model, in which case the inconsistent stiffness and thermal stress load will not happen for elements with low densities, therefore the undesirable parasitic phenomenon can be avoided. The effectiveness of this method has been verified and confirmed in existing studies [54,56]. For the

multi-material model, we adopt the three-phase material model based on a hybrid of the power-law and the Hashin–Shtrikman (HS) interpolation scheme [45], in which case all the physical parameters can be ensured to be within the physically realizable bounds for any densities. Therefore the undesirable parasitic phenomenon is not encountered in the optimization. The effectiveness of this method has been verified in existing studies [45].

4. Numerical examples

In this section, several typical numerical examples are studied to verify the effectiveness of the proposed analysis formulations and topology optimization approach. In the optimization, the penalty factor is set to $p = 3$, the parameter in the K-S function is set to $q = 100$ with the first 12 eigenvalues considered, and the projection parameter θ is set to $\theta = 0.5$. In all the computations, we check the first 12 buckling modes obtained from the analysis to identify potential pseudo buckling modes [21], but we point out that all the computed modes in the following examples are physically-meaningful and thus the pseudo buckling mode problem is not encountered. The lower bound for the additional constraint g_B is set to $\underline{\omega} = 1.2$. Unless stated, a continuation approach was employed for the projection parameter β which starts with $\beta = 2$ and then is raised by $\Delta\beta = 2$ each 25 optimization steps from the 400th iteration, up to the value $\beta = 24$. The method of moving asymptotes (MMA) [57] with an external move limit of 0.1 is adopted to solve all the optimization problems. The stop criterion for the optimizations is that the relative change of the maximum absolute value of design variables of two consecutive iterations is smaller than the tolerance of 0.0001% or the iteration number reaches a limit of 750.

4.1. Single material TO example

In this example, two design domains as illustrated in Fig. 2 are considered. For the first design domain, the width and height of the domain are respectively $L_x = 1.0$ and $L_y = 0.5$; the center node on the left side is pinned and the vertical degree of freedom of the center node on the right side is constrained such that the structure can freely deform in the horizontal direction. Assume that an evenly distributed thermal loading caused by temperature change ΔT is applied and a horizontal mechanical load P is applied to the center of the right side. For the second design domain, the width and height of the domain are respectively $L_x = 1.0$ and $L_y = 0.25$, and the center nodes on the left and right sides are pinned as supports. Assume that an evenly distributed thermal loading ΔT is applied and two horizontal mechanical loadings P_1 and P_2 applied at the center of the domain are considered as two load cases. The magnitudes of P_1 and P_2 are set identical as $|P_1| = |P_2| = 0.001$ but the directions are opposite.

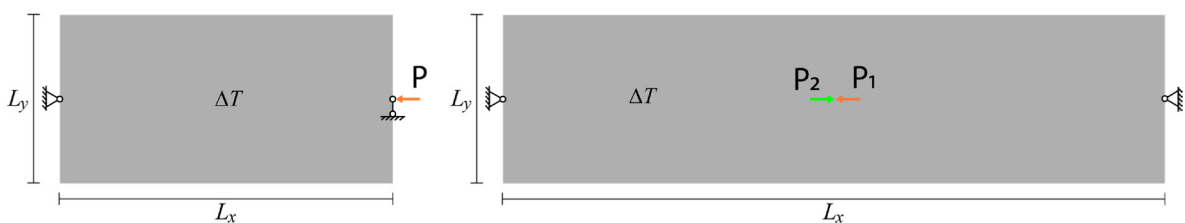


Fig. 2. Design domains considered in Section 4.1.

The discretization is respectively set up with 240×120 square elements and 360×90 square elements for the two design domains, and filter radii of $r_{\min} = 6$ and $r_{\min} = 5$ are adopted respectively in the optimizations. An isotropic material with Young’s modulus $E = 1.0$ ($E_{\min} = 10^{-6}$ for void domain), Poisson’s ratio $\nu = 0.3$, and thermal expansion coefficient $\alpha = 10^{-4}$ is considered. The maximum allowed volume is set to $\bar{V} = 0.25V_0$, where V_0 is the volume of the full design domain; the maximum allowed compliance for each load case is set as $\bar{c} = 3.0c_0$, where c_0 is the compliance of a single load case under the full solid domain.

Since two mechanical load cases with symmetrical loadings are considered for the second design domain, they tend to result in a structure with a symmetric topology with the same buckling resistance capacity for the two load cases. Therefore, based on the BLF maximization model Eq. (29), a min–max formulation [58,59] is employed for the objective function, i.e., to maximize the minimum fundamental BLFs corresponding to the two load cases.

4.1.1. BLF maximization for buckling induced by mechanical loading

(a) Design domain #1

We firstly carry out an optimization with $\Delta T = 0$, i.e., no thermal loading is applied, and the result will be used as a reference for the comparisons with the results obtained by considering thermal loadings. For better illustration, the BLF maximization starts with a compliance-minimized result under only volume constraint, which is similar to the two-phase optimization algorithm proposed in [21]. In addition, the continuation for projection parameter β starts from the 300th iteration and the maximum iteration limit is set to 600 for this example.

The optimized structure for $\Delta T = 0$ is shown in Fig. 3(a) (top). As can be seen, the structure has a fusiform shape with small crossing members distributed inside, which is beneficial for buckling resistance to the mechanical loading. The structure has a fundamental BLF of 6.173 and Fig. 3(a) (bottom) shows the fundamental buckling mode which is a global buckling mode of the entire structure. Note that the colors in the buckling mode figure show the distributions of relative modal strain energy densities for the displacements of the buckling mode.

The optimized structures for $\Delta T = -50$ and $\Delta T = 50$ are shown in Fig. 3(b-c), respectively. It can be seen that the two structures have almost identical topologies, fundamental BLFs, and buckling modes to the optimized structure obtained by $\Delta T = 0$, which indicates that the thermal loadings have a limited effect on the buckling resistance. This is because the structure can freely deform in the horizontal direction and thus thermal loading causes zero stress in the structure, therefore, the buckling resistance capacity of the structure to the mechanical loading is only governed by the structural topology and material properties. This can be verified by the minimum principal stress distributions of the two structures shown in Fig. 4. Compared to the stress caused by mechanical loading, the stress caused by thermal loading is much smaller; in fact, it can be seen that the thermal loadings cause nearly zero stress in the structure and thus has almost no effect on the buckling behavior.

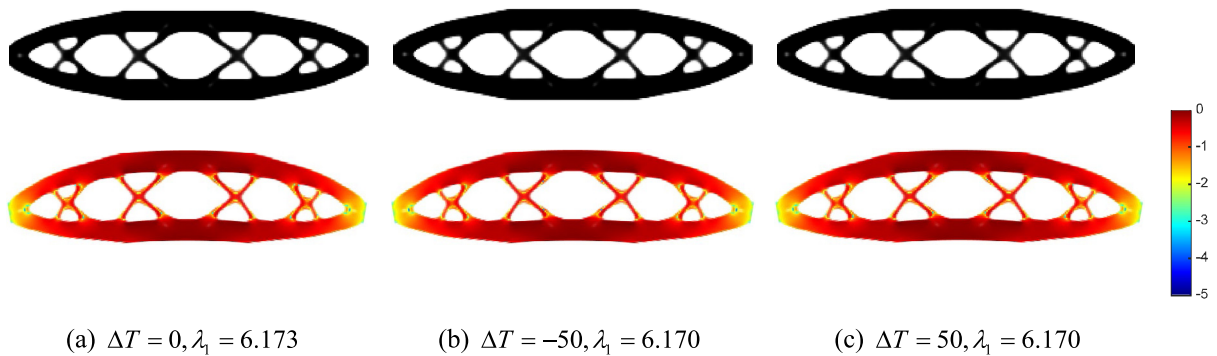


Fig. 3. Optimized structures and corresponding fundamental buckling modes under different thermal loadings. The colors in the figures (second row) denote the distributions of relative modal strain energy densities for the buckling mode. (For interpretation of the references to color in this figure legend, the reader is referred to the web version of this article.)

Taking the case of $\Delta T = 50$ as an example, Fig. 5(a) shows the convergence history of the optimization. The left axis denotes the normalized objective function value while the right axis denotes the constraint function values. The maximum value of all the constraint functions, $g_{\max} (= \max \{g_C, g_V, g_B\})$, is used to illustrate the constraint satisfaction situation in the optimization process; the value of the additional constraint function, g_B , is also included in the diagram to illustrate the influence of thermal loading on buckling. As can be seen, steps appear in the objective function value at the 300th iteration because the projection parameter β starts to increase. Apart from the first several iterations and the iterations near the jumps of β , the maximum value of all the constraint functions, g_{\max} , keeps zero, which means that all the constraints are satisfied. The value of the additional constraint function, g_B , keeps almost constant close to -1 throughout the optimization history, which means that the fundamental BLF for the additional constraint g_B always keeps a sufficiently large value; this also verifies that the thermal loading has no effect on the buckling behavior. Fig. 5(b) shows the convergence history of the first four lowest BLFs ($\lambda_1, \lambda_2, \lambda_3$, and λ_4). In the beginning, the first four BLFs are quite different, but with the progress of optimization, they become close to each other before they divide again for high β values. Also, similar to the objective function value, steps happen at the iterations of jumps of β .

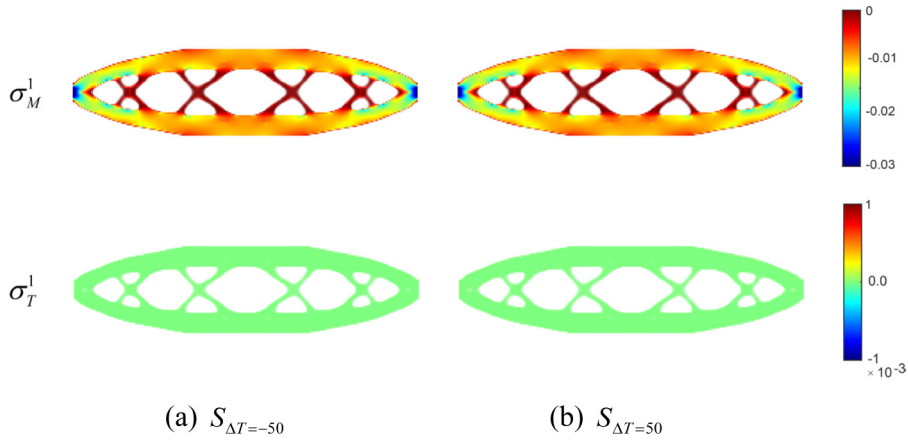


Fig. 4. Minimum principal stress distributions caused by mechanical (σ_M^1) and thermal (σ_T^1) loadings. The colors in the figures denote the distributions of minimum principal stress σ_M^1 and σ_T^1 . (For interpretation of the references to color in this figure legend, the reader is referred to the web version of this article.)

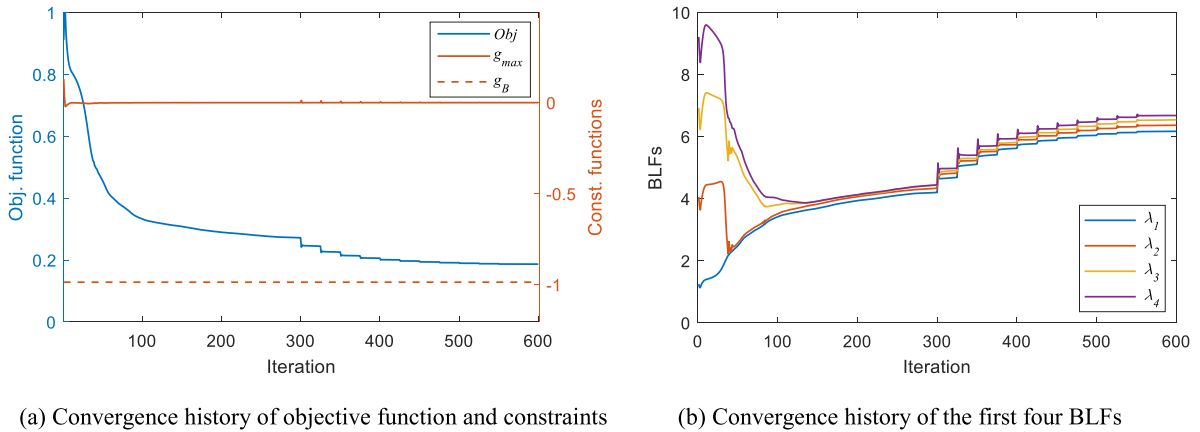


Fig. 5. Convergence history of optimization for the case of $\Delta T = 50$ in Fig. 3.

(b) Design domain #2

Similar to the first design problem, we first carry out an optimization with $\Delta T = 0$, i.e., no thermal loading is applied, and the result will be used as a reference for the comparisons with the results obtained by considering thermal loadings.

The optimized structure for $\Delta T = 0$ is shown in Fig. 6(a). The structure has a symmetric topology and a fundamental BLF of 5.672. Note that the fundamental BLF is taken as the average value of those corresponding to the two load cases (because the structure has a symmetrical topology, the fundamental BLFs corresponding to the two load cases are almost identical). The structure is composed of two fusiform sub-structures with small crossing members distributed inside, which is beneficial to the mechanical buckling resistance. The right figure in Fig. 6(a) shows the fundamental buckling mode of the structure under the first load case. As can be seen, the buckling mode is asymmetrical because under the first load case the left part of the structure is under compression while the right part is under tension. The situation for the second load case is similar but opposite and thus is not shown for brevity.

Next, two other optimizations with $\Delta T = -50$ and $\Delta T = 50$ are carried out and the optimized results are shown in Fig. 6(b–c). For the case of $\Delta T = -50$, the optimized structure has a fundamental BLF of 6.247 that is larger than the result of $\Delta T = 0$, which means that the structure obtained by $\Delta T = -50$ has a larger buckling resistance capacity compared to $\Delta T = 0$; on the contrary, for the case of $\Delta T = 50$, the optimized structure has a fundamental BLF of 4.602 that is smaller than the result of $\Delta T = 0$, indicating that the structure obtained by $\Delta T = 50$ has a

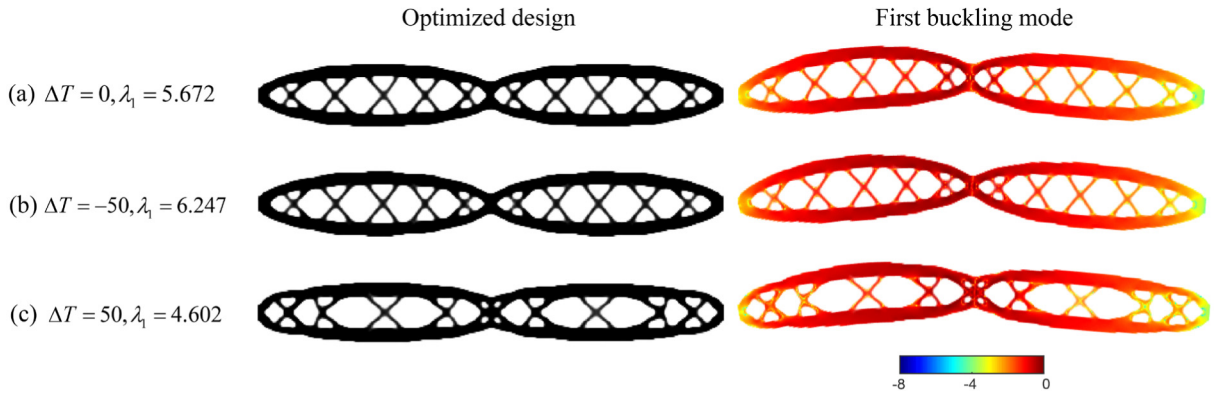


Fig. 6. Optimized structures and corresponding fundamental buckling modes under different thermal loadings. The colors in the buckling mode figures denote the distributions of relative modal strain energy densities for the buckling mode. (For interpretation of the references to color in this figure legend, the reader is referred to the web version of this article.)

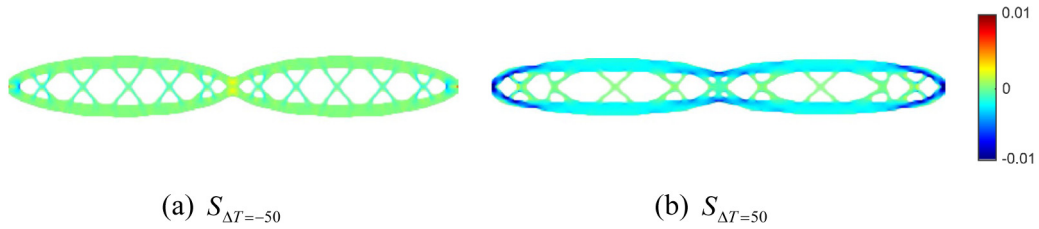


Fig. 7. Minimum principal stress distributions caused by thermal loading. $S_{\Delta T=-50}$ and $S_{\Delta T=50}$ denote the structure obtained under $\Delta T = -50$ and $\Delta T = 50$ respectively and the colors denote minimum principal stress distribution. (For interpretation of the references to color in this figure legend, the reader is referred to the web version of this article.)

smaller buckling resistance capacity compared to $\Delta T = 0$. This can be explained by the minimum principal stress distributions of the two structures caused by the thermal loadings (Fig. 7). It can be seen that the optimized structure for $\Delta T = -50$ is mainly under tension which can alleviate the compression caused by the mechanical loading, hence increasing the buckling resistance capacity; on the contrary, the optimized structure for $\Delta T = 50$ is mainly under compression hence will decrease the buckling resistance capacity to the mechanical loading.

Though thermal loading has a significant effect on the buckling as analyzed above, the change of structural topology also contributes positively to the buckling resistance capacity. Compared to the structure obtained by $\Delta T = 0$, the structures obtained for $\Delta T = -50$ and $\Delta T = 50$ have different topologies. The structure obtained by $\Delta T = -50$ has a narrower middle part, which is beneficial for taking advantage of the tension induced by thermal loading; on the contrary, the structure obtained by $\Delta T = 50$ has a wider middle part, which is beneficial for resisting the evenly distributed compression caused by the thermal loading. Fig. 8 gives the crosschecks of the three structures, which reveals that the optimized structure obtained under a certain ΔT is indeed a better solution than the others.

Take the case of $\Delta T = 50$ as an example, Fig. 9(a) shows the entire convergence history of the optimization while Fig. 9(b) highlights the convergence history of the first 50 iterations. For the first five iterations, the values of g_{\max} are larger than zero and dominated by the value of g_B , which indicates that constraint g_B cannot be satisfied in the beginning. From the 6th iteration, the constraint g_B is satisfied and becomes non-active, and the values of g_{\max} are dominated by the value of g_V . From the 10th iteration, g_{\max} becomes zero, which means that all the constraints are satisfied.

4.1.2. BLF maximization for buckling induced by thermal loading

Next, we investigate the buckling resistance capacity to thermal loading under the effects of mechanical loading for the second design case shown in Fig. 2. Since positive ΔT is not conducive to buckling resistance capacity, here

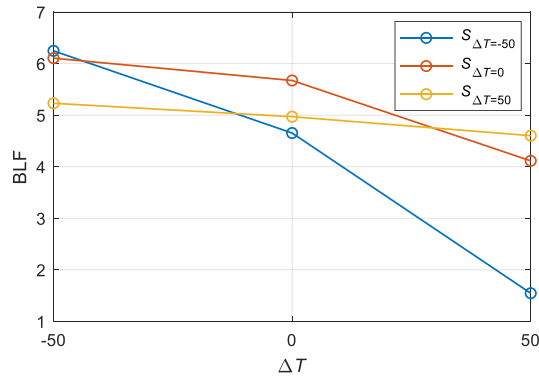


Fig. 8. Crosscheck of optimized structures in Fig. 6.

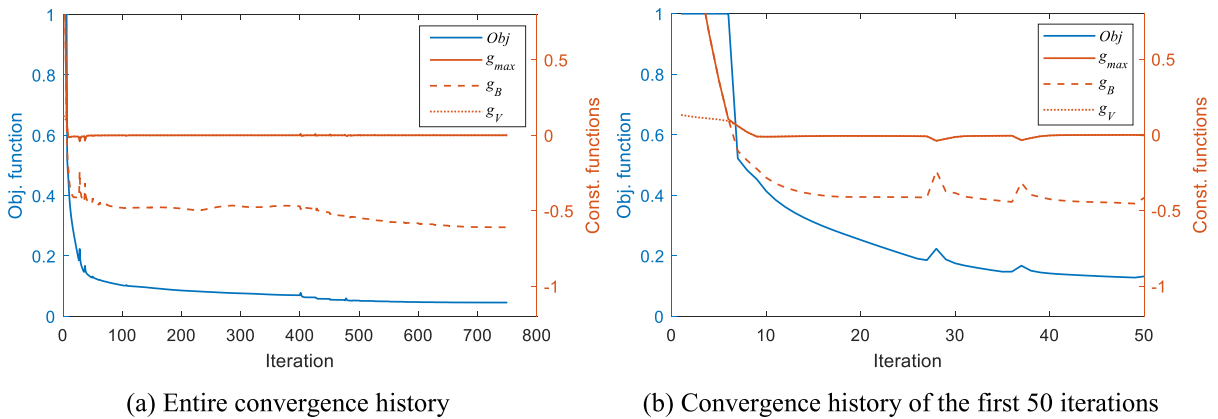


Fig. 9. Convergence history of optimization for the case of $\Delta T = 50$ in Fig. 6.

we only focus on the case of thermal loading caused by positive ΔT . Specifically, we maximize the fundamental BLF associated with a positive $\Delta T = 100$ under a specified mechanical loading.

Different levels of mechanical loadings P_M with respect to a reference magnitude $P_0 = 2.5 \times 10^{-4}$ are adopted to carry out various simulations. The optimized designs and corresponding fundamental BLFs for $P_M = P_0$, $P_M = 3P_0$, and $P_M = 5P_0$ are shown in Fig. 10. As can be seen, the topology patterns and shapes of the optimized structures are quite different from the optimized designs in Section 4.1.1, which indicates that optimizing buckling resistance capacity to mechanical loading and thermal loading are really different and indeed need to be considered as independent problems in practical designs. In addition, the topology of the optimized structures changes, and the fundamental BLFs decrease with the increase of the level of the mechanical loading; this is because larger mechanical loading will cause larger compression in the structures and thus reduce the buckling resistance capacity to thermal loading. Fig. 10 also depicts the fundamental buckling modes of the three structures under the first loading case. As can be seen, the buckling mode of the first structure under a smaller mechanical loading is very close to a symmetric pattern because the buckling mode is mainly governed by the thermal-induced compression that is evenly distributed along the structure. With the increase of mechanical loading, the buckling mode becomes more asymmetrical because the compression caused by mechanical loading tends to have a stronger effect on the buckling.

Apart from the effect of the mechanical loading level, the change of structural topology also has a positive contribution to the buckling resistance capacity against thermal loading. The optimized structure obtained by a relatively small mechanical loading $P_M = P_0$ has a wider middle part that makes the entire structure obtain a generally fusiform shape in order to resist the evenly distributed compression along the structure caused by the thermal loading. The optimized structure obtained for $P_M = 3P_0$ has the same topology as $P_M = P_0$ but a different

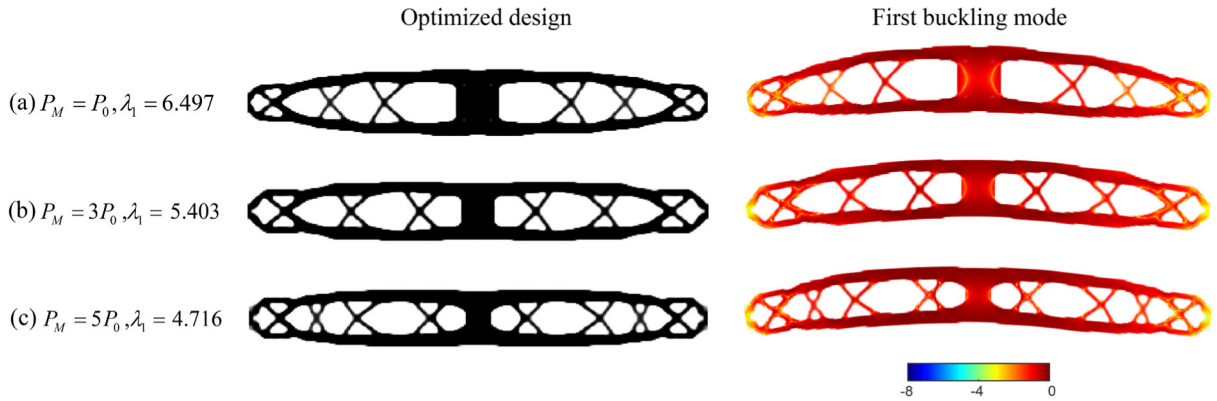


Fig. 10. Optimized structures and corresponding fundamental buckling modes under mechanical loadings. The colors in the buckling mode figures denote the distributions of relative modal strain energy densities for the buckling mode. (For interpretation of the references to color in this figure legend, the reader is referred to the web version of this article.)

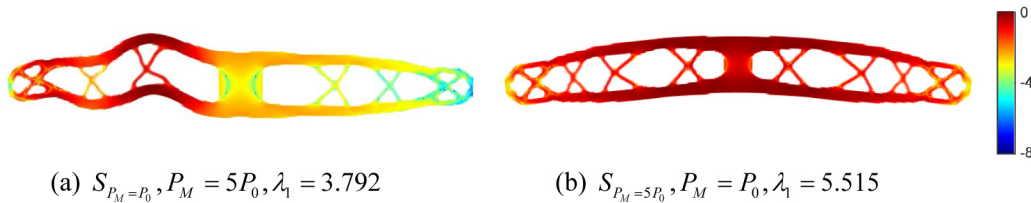


Fig. 11. Buckling modes for crosscheck of optimized structures for $P_M = P_0$ and $P_M = 5P_0$. The colors in the buckling mode figures denote the distributions of relative modal strain energy densities for the buckling mode. (For interpretation of the references to color in this figure legend, the reader is referred to the web version of this article.)

shape. The width of the middle part decreases to make the widths along the structure close and some material migrates from the middle to the sides, especially to the long horizontal members. These shape changes are beneficial for resisting the increased mechanical loading. For the case of $P_M = 5P_0$, the widths along the structure are also close, material in the middle further decreases, and two more crossing members are generated inside the structure to further assist the resistance to the increased mechanical loading.

It has been verified that all the above results pass a crosscheck. As a typical example, Fig. 11 shows the crosscheck results regarding the fundamental BLFs and buckling modes of $S_{P_M=P_0}$ and $S_{P_M=5P_0}$. Under mechanical loading $P_M = 5P_0$, structure $S_{P_M=P_0}$ has a fundamental BLF of 3.792 which is much smaller than 4.716 (Fig. 10(c)); the buckling mode (Fig. 11(a)) indicates that only the left part of the structure buckles instead of the global buckling of the entire structure. For structure $S_{P_M=5P_0}$ under mechanical loading $P_M = P_0$, even though the buckling mode is a global buckling mode of the entire structure (Fig. 11(b)), the fundamental BLF is only 5.515 which is much smaller than 6.497 (Fig. 10(a)).

Take the case of $P_M = 5P_0$ as an example, Fig. 12(a) shows the entire convergence history of the optimization while Fig. 12(b) highlights the convergence history of the first 250 iterations. For the first ten iterations, the values of g_{\max} are larger than zero and dominated by the value of g_B , which indicates that constraint g_B cannot be satisfied in the beginning. From the 11th iteration, constraint g_B can be satisfied and become non-active, and the values of g_{\max} are dominated by the value of g_V . From about the 30th iteration, g_{\max} becomes zero, which means that all the constraints are satisfied. From about the 230th iteration, constraint g_C also becomes active, and at the same time, the value of g_B starts to increase. At the jumps of β , constraint g_B becomes active tentatively but decreases generally with the progress of optimization and keeps non-active at the end.

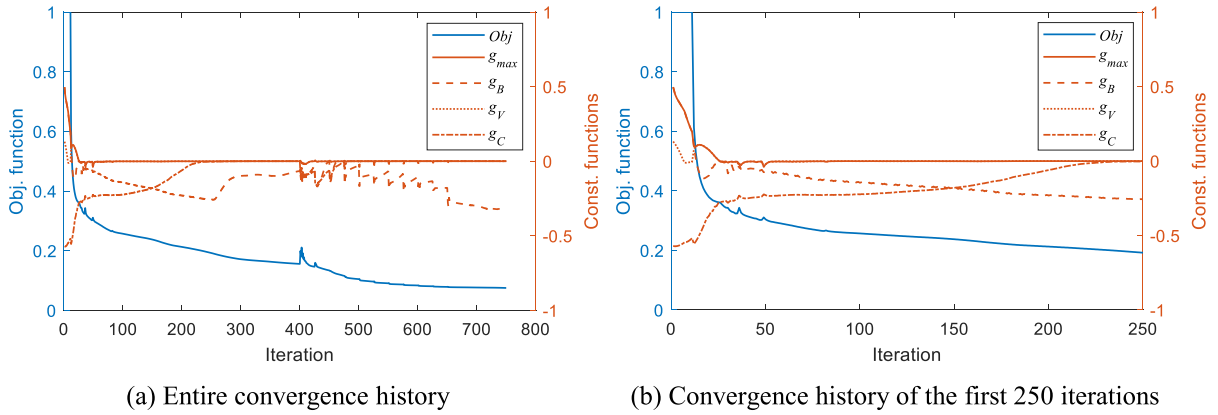


Fig. 12. Convergence history of optimization for the case of $P_M = 5P_0$ in Fig. 10.

4.2. Multiple material TO examples

In this section, the developed two-material topology optimization model is adopted to design active or prestressed structures with better buckling resistance capacity to mechanical loading (i.e., model #2 is adopted for the buckling analysis). Fig. 13 gives an illustrative example of the optimal design procedure. The cantilever structure is made of two materials: passive material and active material. It is assumed that the passive material has a zero while the active material has a non-zero thermal expansion coefficient and thus the active material can be driven actively by temperature variation. Thermal expansion is used as a strategy here to simulate various linear-strain-based actuation effects such as shape memory alloys (SMA) and piezoelectric (PZT) materials. The expansion or contraction of the active material may affect the structural responses (e.g., stress) of the entire structure, that is to say, the structural responses can be actively controlled by actively and strategically changing the temperature. Apart from mimicking active structures, as a special case, the model can also be used to mimic prestressed structures, say the components consisting of active material can be assumed to be some prestressed components like cable tendons, in which case a negative temperature variation will be adopted.

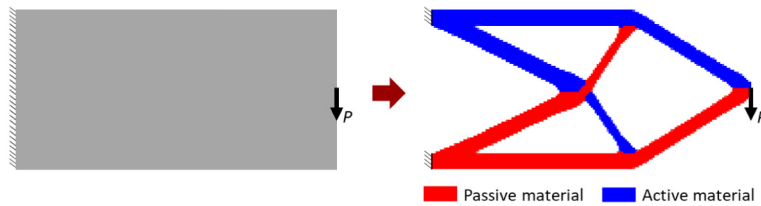


Fig. 13. Illustration for active and prestressed structure modeling.

In the following computations, the passive material and active material are assumed to have the same Young’s modulus $E = 1.0$ ($E_{min} = 10^{-6}$ for void domain) and Poisson’s ratio $\nu = 0.3$ but different thermal expansion coefficients; the active material is assumed to have a non-zero thermal expansion coefficient $\alpha = 0.001$ while the passive material is assumed to have a zero thermal expansion coefficient. Different ΔT denote different levels of actuation or prestress loads applied to the structure. Unless stated, other parameters are set the same as those in Section 4.1.

4.2.1. BLF maximization of active structure

The second design problem shown in Fig. 2 is restudied here to design an active structure. We first need to design a passive structure for reference. The design of the passive structure is actually the same as the single-material optimal design in Section 4.1.1 for $\Delta T = 0$. Therefore, the structure in Fig. 6(a) is used here for the reference comparison with the optimized active structures. Note that for the optimization of active structures, the maximum

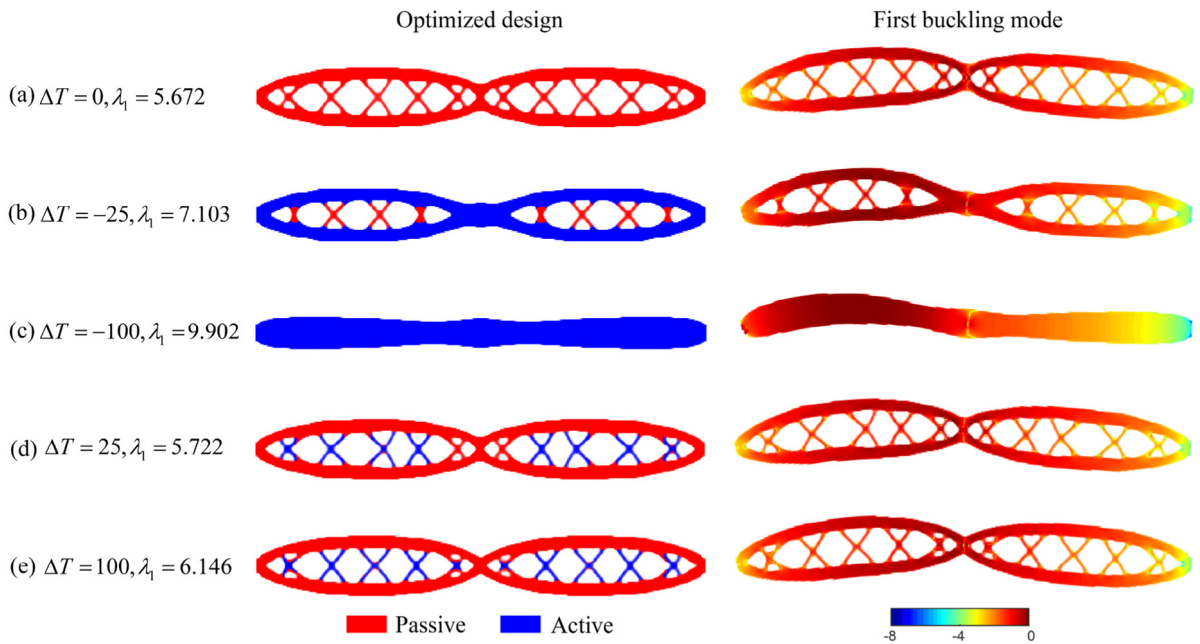


Fig. 14. Optimized structures and corresponding fundamental buckling modes under different actuation loads. The colors in the buckling mode figures denote the distributions of relative modal strain energy densities for the buckling mode. (For interpretation of the references to color in this figure legend, the reader is referred to the web version of this article.)

allowed volume is also set to $\bar{V} = 0.25V_0$, and no limit is enforced for the volume of a single material occupation, i.e., the optimizer can freely select materials as long as the structural total volume $V (= V_p + V_a) \leq 0.25V_0$.

First, two optimizations with $\Delta T = -25$ and -100 are carried out and the optimized structures are shown in Fig. 14(b–c). The structure obtained for $\Delta T = -25$ consists of two fusiform sub-structures with small crossing members distributed inside, which is similar to the passive structure; however, the crossing members at the two ends and near the middle are merged into single vertical members and the entire structure is thinner than the passive structure, especially for the middle part. The active material mainly distributes at the outside horizontal members, which is beneficial for the actuation to induce tensile stress in the structure to enhance the buckling resistance capacity to the mechanical loading. This can be illustrated by the comparison of minimum principal stress distributions (under the first load case) with and without actuation shown in Fig. 15(a). Without actuation, the left part of the structure is under compression but turns under tension when actuation is applied. The case for the second load case is similar. For this reason, the structure has a larger fundamental BLF of 7.103. The optimized structure for $\Delta T = -100$ has a significantly different topology than the previous two structures. The entire structure forms a straight bar made of active material in order to fully utilize the relatively large actuation load for enhancing the buckling resistance capacity. This form gives the structure a much larger fundamental BLF of 9.902.

Next, two optimizations with $\Delta T = 25$ and 100 are carried out and the optimized structures are shown in Fig. 14(d–e). The two structures have similar topologies and the inside crossing members are made of mainly active materials, which results in larger fundamental BLFs. This is because under a positive ΔT , the active material will expand and thus the crossing members can serve as actuators to push the horizontal members; this will introduce roughly horizontal tensile stress into the structure, which alleviates the compression caused by the mechanical loading and thus increases the buckling resistance capacity. This can be illustrated by the minimum principal stress distributions (under the first load case) with and without actuation shown in Fig. 15(b). Without actuation, the left part of the structure is under relatively large compression, but the compression stress reduces when actuation is applied.

Note that all the solutions pass the crosscheck, which indicates that they are indeed better structures compared to others under the ΔT they were optimized for.

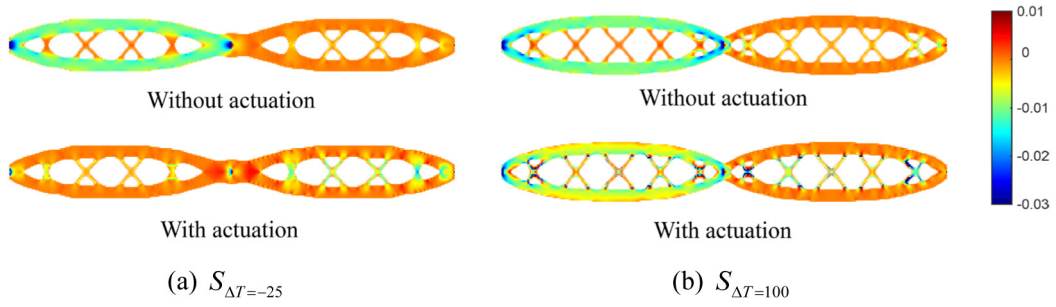


Fig. 15. Minimum principal stress distributions with and without actuation loads. The colors denote minimum principal stress distribution. (For interpretation of the references to color in this figure legend, the reader is referred to the web version of this article.)

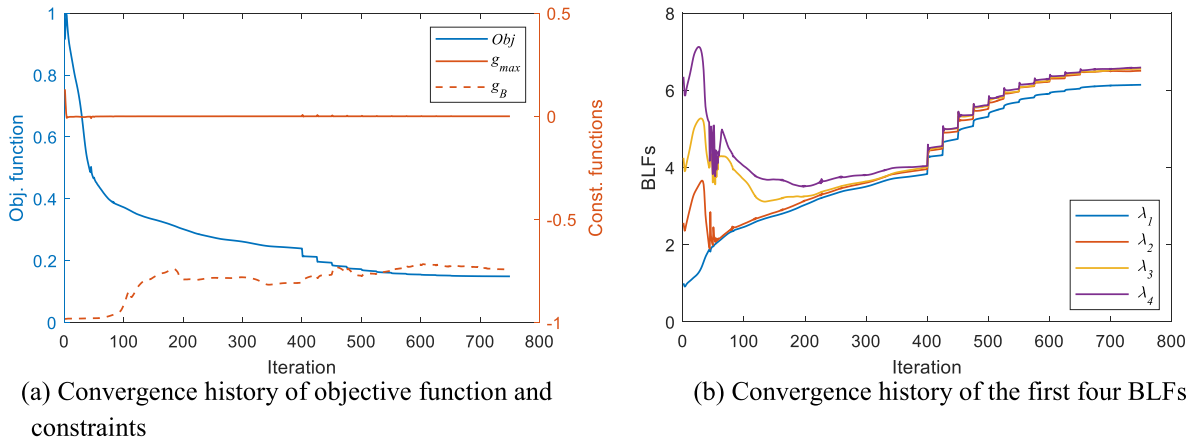


Fig. 16. Convergence history of optimization for the case of $\Delta T = 100$ in Fig. 14.

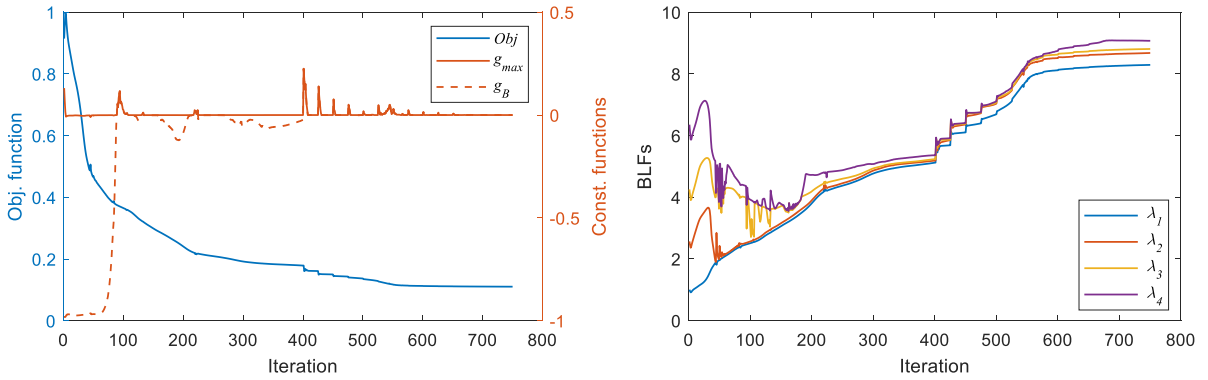
As a typical example, Fig. 16 shows the convergence history of optimization and the first four lowest BLFs for the case of $\Delta T = 100$. As can be seen, the optimization process is quite stable; the additional constraint g_B starts from a value close to -1 and gradually increases to around -0.75 in the first several iterations but does not change too much from about the 200th iteration until the end. This means that the additional constraint g_B never becomes active during the optimization, which is because the actuation load is not large enough to trigger the additional constraint g_B .

Next, we adopt a larger actuation load $\Delta T = 1000$ to carry out a test. Fig. 17 shows the convergence history of the optimization and the first four lowest BLFs. As can be seen, the additional constraint g_B becomes active from around the 100th iteration; even though sometimes becomes non-active during the optimization, it stays active at the end. Fig. 18 shows the optimized structure together with the fundamental buckling mode. Active material still distributes inside the structure and the horizontal members outside are curved instead of straight like in previous optimized structures, which is beneficial to avoid the buckling caused by the sufficiently large actuation load.

4.2.2. BLF maximization of prestressed structure

In this example, we use the two-material model to design a prestressed structure. The design domain is shown in Fig. 19. The horizontal size L_x is set to unit length and the vertical size L_y is set to $L_y = 0.2L_y$. The middle part is a void domain that will not be considered in the optimization. The left and right nodes in the bottom are pinned and small regions near the bottom sides of the void domain are fixed. A distributed line load having the same width as the void domain is applied on the top of the structure. A narrow area directly under the line load is fixed to be fully solid in the optimization.

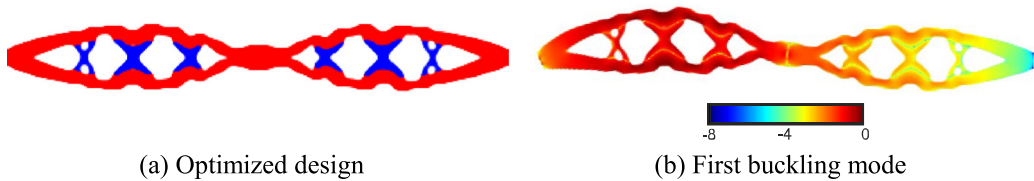
A compliance-minimized passive structure is firstly designed by using 10% volume of the full domain ($L_y \times L_y$). Then, 5% more material is allowed to be added to enhance the structural stability by using a fixed prestress



(a) Convergence history of objective function and constraints

(b) Convergence history of the first four BLFs

Fig. 17. Convergence history of optimization for $\Delta T = 1000$.



(a) Optimized design

(b) First buckling mode

Fig. 18. Optimized structure and corresponding fundamental buckling mode for $\Delta T = 1000$. The colors in the buckling mode figures denote the distributions of relative modal strain energy densities for the buckling mode. (For interpretation of the references to color in this figure legend, the reader is referred to the web version of this article.)

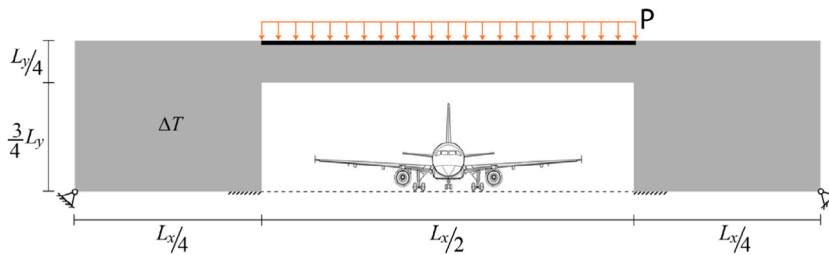


Fig. 19. Design domain of prestressed shelter structure.

load of $\Delta T = -100$. Different upper bounds for the active material occupation are adopted to carry out various optimizations. First, we perform the optimization without enforcing active material occupation limit and obtain an optimized structure shown in Fig. 20(a). In this structure, the active material takes up about 49.3% of the total structural volume and mainly distributes in three regions: the two long thin inclined members at the two sides, the top and bottom chords of the horizontal truss in the middle, and two short-inclined members near the middle bottom supports. Under the applied loading, the top chord of the middle horizontal truss will carry severe compression stress; the prestress load will introduce contraction forces (i.e., tensile stress) into the first two areas to alleviate the compression in the top chord, and thus increase the buckling resistance capacity. Also, the two long thin inclined members at the sides can serve as stabilizing tension members to stabilize the entire structure. For the two short inclined tensioned members near the middle supports, their functions are similar to the two long thin inclined members to stabilize the middle vertical columns. In addition, the prestress in the long-inclined members is deviated by two deviator bars from inclined directions to horizontal directions applied to the top chord of the middle truss.

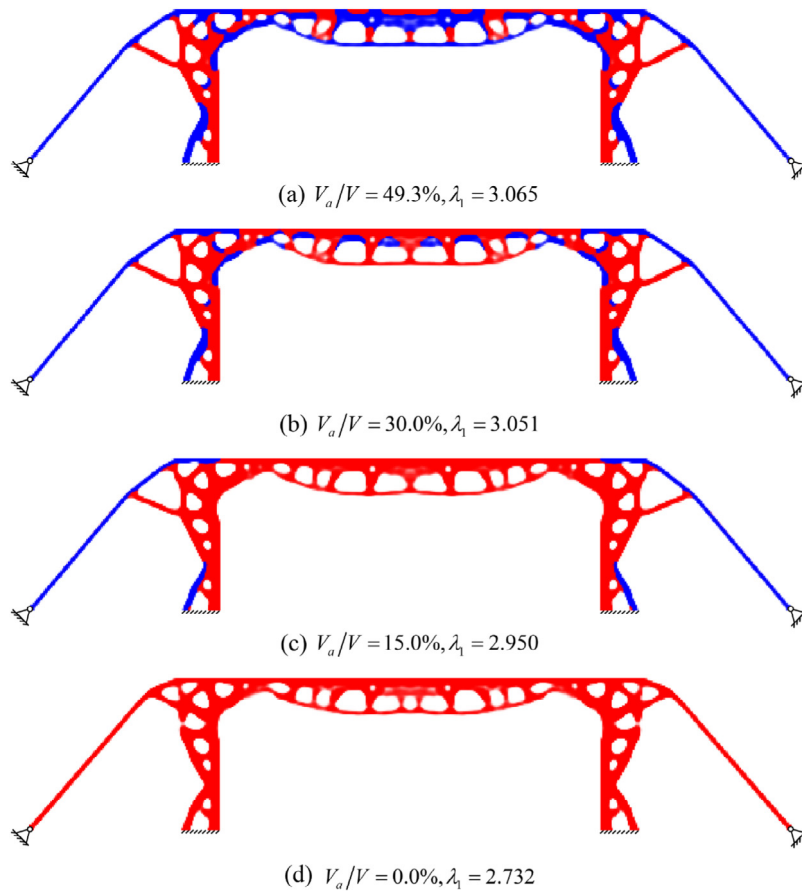


Fig. 20. Optimized structures under different active material volume occupation bounds.

Next, we adopted different upper bounds of 30% and 15% (i.e., V_a/V) for the active material occupation to carry out two optimizations, and the corresponding optimized designs are shown in Fig. 20(b–c). As can be seen, the topologies of the obtained structures are similar to the previous structure, but with the decrease of the upper bounds, the active material distributed in the middle horizontal truss becomes less and less and the active material is mainly used for the inclined members at the two sides, which implies that the tension in the inclined members has a more significant contribution to structural stability.

The optimized passive structure without prestress is shown in Fig. 20(d). The topology of the passive structure is similar to the prestressed structures, but two main differences can be observed. First, the inclined members at the sides are thicker than those of the prestressed designs; this is because no prestress exists in the inclined members, and a larger member cross-section size is required to provide enough lateral support for structural stability and also ensure its own stability. Second, the four deviator bars at the two sides are shorter and closer to the end of the middle truss; this might be because longer deviator bars in the passive structure have little effect on the lateral supporting of the middle columns because the long-inclined members have no prestress, which leads to the result that the additional material is used in other parts of the structure to better enhance structural stability. Comparisons indicate that all the topology-optimized prestressed designs achieve larger fundamental BLFs, i.e., higher stability, than the optimized passive design, which verifies the effectiveness of the proposed approach and also demonstrates the benefit of using prestress to enhance structural stability. Notably, a truss with better stability enhanced by externally prestressed cables (Fig. 21) that is similar to the structure in Fig. 20(c) has been proposed and verified by a recent study in [60].

To further demonstrate the influence of prestress on structural stability, the optimized structure in Fig. 20(c) is adopted as an illustrative example. Fig. 22 shows the fundamental buckling modes of the structure with and

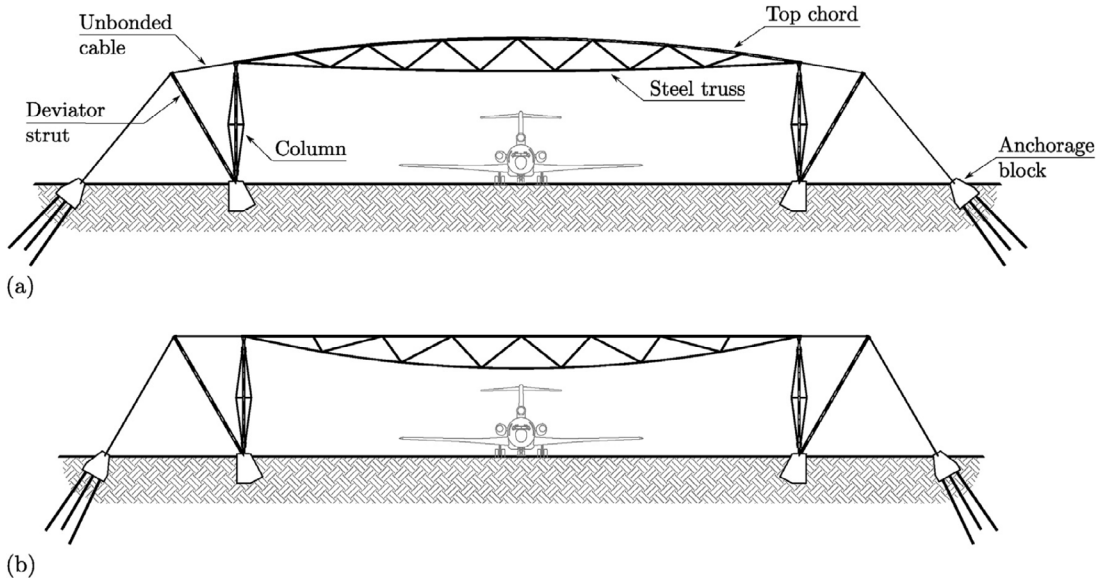


Fig. 21. Roof truss stabilized with externally anchored prestressed cables.
 Source: Reprinted with permission from Elsevier, from Ref. [60].



Fig. 22. Fundamental buckling modes of optimized structure Fig. 20(c) with and without prestress. The colors in the buckling mode figures denote the distributions of relative modal strain energy densities for the buckling mode. (For interpretation of the references to color in this figure legend, the reader is referred to the web version of this article.)

without prestress. As can be seen, without prestress, the buckling happens at the middle horizontal truss because the top chord is under severe compression stress and thus easy to buckle, which leads to a much smaller BLF of 1.799. With prestress, the buckling is a global mode of the entire structure; this is because the prestress in the inclined members at the two sides will introduce tension into the top chord of the middle truss and thus alleviate the compression caused by the mechanical loading, which increases the buckling resistance capacity. This can be observed by the minimum principal stress distributions of the two structures (Fig. 23). Without prestress, a large part of the top chord of the middle truss is under compression, while the maximum compression stress and area under compression significantly decrease for the structure with prestress.



Fig. 23. Minimum principal stress distributions of optimized structure Fig. 20(c) with and without prestress. The colors denote minimum principal stress distribution. (For interpretation of the references to color in this figure legend, the reader is referred to the web version of this article.)

5. Concluding remarks

This study proposes a topology optimization framework to maximize linearized buckling capacity under thermo-mechanical loading using decoupled analysis models. Unlike the conventional coupled analysis model, the decoupled analysis models allow us to independently study the buckling induced by mechanical or thermal loading, i.e., buckling induced by mechanical loading under a specified thermal loading or buckling induced by thermal loading under a specified mechanical loading.

A topology optimization model to maximize the fundamental buckling load factor for single-material structure is first developed. The numerical examples indicate that optimizing buckling capacity induced by mechanical loading and induced by thermal loading lead to quite different optimized topologies and thus they indeed need to be considered as independent problems in practical designs, which demonstrates the necessity and effectiveness of the proposed decoupled analysis formulations for handling such problems. Further, a multi-material topology optimization model is developed to design active structures and prestressed structures with better stability regarding mechanical loading, assuming that thermal loading is used as a strategy to denote linear-strain-based actuation effects and prestress loading. Numerical examples indicate that, compared to topology-optimized passive structures, the buckling capacity of topology-optimized active structures and prestressed structures can be enhanced. The optimized topology of the active or prestressed structure may or may not be the same as that of the corresponding passive structure, depending on the actuation/prestress load level or active material occupation ratio.

Based on the study, the following points are highlighted for future investigations on topology optimization considering buckling/stability criterion:

- The decoupled analysis models allow one to independently study the buckling induced by mechanical loading and the buckling induced by thermal loading, which has a clearer physical meaning for practical design.
- The single-material model allows one to perform the topology optimization considering stability criterion regarding buckling induced by mechanical loading under a specified thermal loading or buckling induced by thermal loading under a specified mechanical loading.
- The multi-material model allows one to perform the topology optimization of active structures made of structural material and linear-strain-based actuating material (e.g., SMA, PZT) to achieve better stability regarding mechanical loading.
- The multi-material model allows one to perform the topology optimization of prestressed structures composed of prestressed components (e.g., prestressed cable tendons) to achieve better stability regarding mechanical loading.

Finally, we remark that though the current study is to maximize the buckling load factor in the optimization and based on a 2D plane stress assumption, the proposed formulations can be straightforwardly extended to other buckling-constrained problems and plane strain/3D problems under thermo-mechanical loading; also, though the multi-material model is used to design active and prestressed structures in this study, it can be extended to design multi-material passive structures.

Declaration of competing interest

The authors declare that they have no known competing financial interests or personal relationships that could have appeared to influence the work reported in this paper.

Data availability

No data was used for the research described in the article.

Acknowledgments

Yafeng Wang is supported by the European Union's Horizon 2020 research and innovation programme under the Marie Skłodowska-Curie grant agreement No 899987. Ole Sigmund is supported by the Villum Foundation through the Villum Investigator Project InnoTop. The authors are grateful to Dr. Federico Ferrari for several fruitful discussions on the paper and for providing the 250-line Matlab code for linearized buckling analysis.

Appendix. Sensitivity analysis

A.1. Sensitivity of volume

For the single-material model, $V = \sum_e V_e \tilde{x}_e$, then

$$\frac{\partial V}{\partial \tilde{x}_e} = V_e \tag{A.1}$$

For the multi-material model, $V_a = \sum_e V_e \tilde{\xi}_e \tilde{\eta}_e$, $V_p = \sum_e V_e \tilde{\xi}_e (1 - \tilde{\eta}_e)$, then

$$\frac{\partial V_a}{\partial \tilde{\xi}_e} = V_e \tilde{\eta}_e, \frac{\partial V_a}{\partial \tilde{\eta}_e} = V_e \tilde{\xi}_e, \frac{\partial V_p}{\partial \tilde{\xi}_e} = V_e (1 - \tilde{\eta}_e), \frac{\partial V_p}{\partial \tilde{\eta}_e} = -V_e \tilde{\xi}_e \tag{A.2}$$

$$\frac{\partial V}{\partial \tilde{\xi}_e} = V_e \tilde{\eta}_e + V_e (1 - \tilde{\eta}_e) = V_e, \frac{\partial V}{\partial \tilde{\eta}_e} = V_e \tilde{\xi}_e - V_e \tilde{\xi}_e = 0 \tag{A.3}$$

A.2. Sensitivity of compliance

The compliance is defined as $C = \mathbf{P}_m^T \mathbf{U}_m$, then through the adjoint method,

$$\frac{\partial C}{\partial \tilde{x}_e} = \frac{\partial}{\partial \tilde{x}_e} [\mathbf{P}_m^T \mathbf{U}_m + \boldsymbol{\chi}_m^T (\mathbf{K} \mathbf{U}_m - \mathbf{P}_m)] = \mathbf{P}_m^T \frac{\partial \mathbf{U}_m}{\partial \tilde{x}_e} + \boldsymbol{\chi}_m^T \left(\frac{\partial \mathbf{K}}{\partial \tilde{x}_e} \mathbf{U}_m + \mathbf{K} \frac{\partial \mathbf{U}_m}{\partial \tilde{x}_e} \right) \tag{A.4}$$

To eliminate the terms containing $\frac{\partial \mathbf{U}_m}{\partial \tilde{x}_e}$, the adjoint vectors $\boldsymbol{\chi}_m$ can be calculated as $\boldsymbol{\chi}_m = -\mathbf{U}_m$, then

$$\frac{\partial C}{\partial \tilde{x}_e} = -\mathbf{U}_m^T \frac{\partial \mathbf{K}}{\partial \tilde{x}_e} \mathbf{U}_m \tag{A.5}$$

where $\frac{\partial \mathbf{K}}{\partial \tilde{x}_e} = \frac{\partial h_e}{\partial \tilde{x}_e} \int_{V_e} \mathbf{B}_e^T \mathbf{D}_0 \mathbf{B}_e dV$. For the single-material model, interpolation function $h_e(\tilde{x}_e)$ is given by Eq. (20). For the multi-material model, \tilde{x}_e denotes $\tilde{\xi}_e$ or $\tilde{\eta}_e$ and $h_e(\tilde{x}_e)$ is given by Eq. (34).

A.3. Sensitivity of BLF

The sensitivity of the K-S function Eq. (23) is given by

$$\frac{\partial J^{KS}[\mu_i]}{\partial \tilde{x}_e} = \frac{\sum_{i \in \Theta} e^{q(\mu_i - \mu_1)} \frac{\partial \mu_i}{\partial \tilde{x}_e}}{\sum_{i \in \Theta} e^{q(\mu_i - \mu_1)}} \tag{A.6}$$

Next, $\frac{\partial \mu_i}{\partial \tilde{x}_e}$ will be calculated. Without loss of generality, we take analysis model #2 as an example for the following derivations and assume that the thermal expansion coefficient is a function of the physical-field variables, i.e., $\alpha_e = \alpha_e(\tilde{x}_e)$, in order to generalize the sensitivity formulations to be able to apply to both the single- and multiple-material models.

For an arbitrary eigenvalue $\lambda_i (=1/\mu_i)$ with associated eigenvector $\boldsymbol{\varphi}_i$, multiplying $\boldsymbol{\varphi}_i$ on both sides of Eq. (22) gives

$$\boldsymbol{\varphi}_i^T [\mu_i (\mathbf{K} + \mathbf{G}_t) + \mathbf{G}_m] \boldsymbol{\varphi}_i + \boldsymbol{\chi}_m^T (\mathbf{K} \mathbf{U}_m - \mathbf{P}_m) + \boldsymbol{\chi}_t^T (\mathbf{K} \mathbf{U}_t - \mathbf{P}_t) = 0 \tag{A.7}$$

where $\boldsymbol{\chi}_m$ and $\boldsymbol{\chi}_t$ are the vectors of the adjoint variables. Then the sensitivity of μ_i with respect to physical-field variable \tilde{x}_e can be calculated by differentiating Eq. (A.7) as

$$\begin{aligned} & 2 \frac{\partial \boldsymbol{\varphi}_i}{\partial \tilde{x}_e} [\mu_i (\mathbf{K} + \mathbf{G}_t) + \mathbf{G}_m] \boldsymbol{\varphi}_i + \boldsymbol{\varphi}_i^T \left[\mu_i \left(\frac{\partial \mathbf{K}}{\partial \tilde{x}_e} + \frac{\partial \mathbf{G}_t}{\partial \tilde{x}_e} + \frac{\partial \mathbf{G}_t}{\partial \mathbf{U}_t} \frac{\partial \mathbf{U}_t}{\partial \tilde{x}_e} \right) + \frac{\partial \mu_i}{\partial \tilde{x}_e} (\mathbf{K} + \mathbf{G}_t) + \frac{\partial \mathbf{G}_m}{\partial \tilde{x}_e} + \frac{\partial \mathbf{G}_m}{\partial \mathbf{U}_m} \frac{\partial \mathbf{U}_m}{\partial \tilde{x}_e} \right] \boldsymbol{\varphi}_i \\ & + \boldsymbol{\chi}_m^T \left(\frac{\partial \mathbf{K}}{\partial \tilde{x}_e} \mathbf{U}_m + \mathbf{K} \frac{\partial \mathbf{U}_m}{\partial \tilde{x}_e} \right) + \boldsymbol{\chi}_t^T \left(\frac{\partial \mathbf{K}}{\partial \tilde{x}_e} \mathbf{U}_t + \mathbf{K} \frac{\partial \mathbf{U}_t}{\partial \tilde{x}_e} - \frac{\partial \mathbf{P}_t}{\partial \tilde{x}_e} \right) = 0 \end{aligned} \tag{A.8}$$

According to Eq. (22), the first term of Eq. (A.8) equals zero. Rearranging the items gives

$$\begin{aligned} \boldsymbol{\varphi}_i^T \left[\mu_i \left(\frac{\partial \mathbf{K}}{\partial \tilde{x}_e} + \frac{\partial \mathbf{G}_t}{\partial \tilde{x}_e} \right) + \frac{\partial \mathbf{G}_m}{\partial \tilde{x}_e} \right] \boldsymbol{\varphi}_i + \frac{\partial \mu_i}{\partial \tilde{x}_e} \boldsymbol{\varphi}_i^T (\mathbf{K} + \mathbf{G}_t) \boldsymbol{\varphi}_i + \boldsymbol{\chi}_m^T \frac{\partial \mathbf{K}}{\partial \tilde{x}_e} \mathbf{U}_m + \boldsymbol{\chi}_t^T \left(\frac{\partial \mathbf{K}}{\partial \tilde{x}_e} \mathbf{U}_t - \frac{\partial \mathbf{P}_t}{\partial \tilde{x}_e} \right) \\ + \left(\boldsymbol{\varphi}_i^T \frac{\partial \mathbf{G}_m}{\partial \mathbf{U}_m} \boldsymbol{\varphi}_i + \boldsymbol{\chi}_m^T \mathbf{K} \right) \frac{\partial \mathbf{U}_m}{\partial \tilde{x}_e} + \left(\boldsymbol{\varphi}_i^T \frac{\partial \mathbf{G}_t}{\partial \mathbf{U}_t} \boldsymbol{\varphi}_i + \boldsymbol{\chi}_t^T \mathbf{K} \right) \frac{\partial \mathbf{U}_t}{\partial \tilde{x}_e} = \mathbf{0} \end{aligned} \quad (\text{A.9})$$

To eliminate the terms containing $\frac{\partial \mathbf{U}_m}{\partial \tilde{x}_e}$ and $\frac{\partial \mathbf{U}_t}{\partial \tilde{x}_e}$, the adjoint vectors $\boldsymbol{\chi}_m$ and $\boldsymbol{\chi}_t$ are calculated by

$$\mathbf{K} \boldsymbol{\chi}_m = -\boldsymbol{\varphi}_i^T \frac{\partial \mathbf{G}_m}{\partial \mathbf{U}_m} \boldsymbol{\varphi}_i, \quad \mathbf{K} \boldsymbol{\chi}_t = -\mu_i \boldsymbol{\varphi}_i^T \frac{\partial \mathbf{G}_t}{\partial \mathbf{U}_t} \boldsymbol{\varphi}_i \quad (\text{A.10})$$

By combining Eqs. (A.9) and (A.10), the sensitivity of μ_i is given by

$$\frac{\partial \mu_i}{\partial \tilde{x}_e} = \frac{-\boldsymbol{\varphi}_i^T \left[\mu_i \left(\frac{\partial \mathbf{K}}{\partial \tilde{x}_e} + \frac{\partial \mathbf{G}_t}{\partial \tilde{x}_e} \right) + \frac{\partial \mathbf{G}_m}{\partial \tilde{x}_e} \right] \boldsymbol{\varphi}_i - \boldsymbol{\chi}_m^T \frac{\partial \mathbf{K}}{\partial \tilde{x}_e} \mathbf{U}_m - \boldsymbol{\chi}_t^T \left(\frac{\partial \mathbf{K}}{\partial \tilde{x}_e} \mathbf{U}_t - \frac{\partial \mathbf{P}_t}{\partial \tilde{x}_e} \right)}{\boldsymbol{\varphi}_i^T (\mathbf{K} + \mathbf{G}_t) \boldsymbol{\varphi}_i} \quad (\text{A.11})$$

In the above formulation,

$$\frac{\partial \mathbf{K}}{\partial \tilde{x}_e} = \frac{\partial h_e}{\partial \tilde{x}_e} \int_{V_e} \mathbf{B}_e^T \mathbf{D}_0 \mathbf{B}_e dV \quad (\text{A.12})$$

$$\frac{\partial \mathbf{P}_t}{\partial \tilde{x}_e} = \frac{\partial h_e}{\partial \tilde{x}_e} \int_{V_e} \mathbf{B}_e^T \mathbf{D}_0 \boldsymbol{\varepsilon}_{\Delta t, e} dV + \frac{\partial \alpha_e}{\partial \tilde{x}_e} \int_{V_e} \mathbf{B}_e^T \mathbf{D}_e \boldsymbol{\Phi} \Delta T_e dV \quad (\text{A.13})$$

$$\frac{\partial \mathbf{G}_m}{\partial \tilde{x}_e} = \int_{V_e} \mathbf{B}_e^T \frac{\partial \mathbf{S}_m}{\partial \tilde{x}_e} \mathbf{B}_e dV \quad (\text{A.14})$$

where $\mathbf{S}_m = \mathbf{I} \otimes \hat{\boldsymbol{\sigma}}_m$ with \mathbf{I} being the identity matrix and $\hat{\boldsymbol{\sigma}}_m$ the stress tensor caused by the mechanical loading. Then, $\frac{\partial \mathbf{S}_m}{\partial \tilde{x}_e}$ is given by

$$\frac{\partial \mathbf{S}_m}{\partial \tilde{x}_e} = \mathbf{I} \otimes \frac{\partial \hat{\boldsymbol{\sigma}}_m}{\partial \tilde{x}_e} \quad (\text{A.15})$$

The sensitivity of stress vector $\boldsymbol{\sigma}_m$ with respect to \tilde{x}_e can be expressed as

$$\frac{\partial \boldsymbol{\sigma}_m}{\partial \tilde{x}_e} = \frac{\partial h_e}{\partial \tilde{x}_e} \mathbf{D}_0 \mathbf{B}_e \mathbf{U}_m \quad (\text{A.16})$$

Similarly,

$$\frac{\partial \mathbf{G}_t}{\partial \tilde{x}_e} = \int_{V_e} \mathbf{B}_e^T \frac{\partial \mathbf{S}_t}{\partial \tilde{x}_e} \mathbf{B}_e dV \quad (\text{A.17})$$

$$\frac{\partial \mathbf{S}_t}{\partial \tilde{x}_e} = \mathbf{I} \otimes \frac{\partial \hat{\boldsymbol{\sigma}}_t}{\partial \tilde{x}_e} \quad (\text{A.18})$$

$$\frac{\partial \boldsymbol{\sigma}_t}{\partial \tilde{x}_e} = \frac{\partial h_e}{\partial \tilde{x}_e} \mathbf{D}_0 \mathbf{B}_e \mathbf{U}_t - \frac{\partial h_e}{\partial \tilde{x}_e} \mathbf{D}_0 \mathbf{B}_e \boldsymbol{\varepsilon}_{\Delta t, e} - \frac{\partial \alpha_e}{\partial \tilde{x}_e} \mathbf{D}_e \boldsymbol{\Phi} \Delta T_e \quad (\text{A.19})$$

For the single-material model, suitable interpolation function $h_e(\tilde{x}_e)$ for Young's modulus is given in Eq. (20), and thermal expansion coefficient α_e is a constant for all the elements (i.e., $\frac{\partial \alpha_e}{\partial \tilde{x}_e} = 0$). For the multi-material model, \tilde{x}_e denotes $\tilde{\xi}_e$ or $\tilde{\eta}_e$, and interpolation functions for $\alpha_e(\tilde{x}_e)$ and $h_e(\tilde{x}_e)$ are given in Eqs. (32) and (34) respectively.

The sensitivities for the buckling analysis based on model #3 and additional constraint g_B can be analyzed similarly.

References

- [1] Aykut Kentli, Topology optimization applications on engineering structures, in: Truss and Frames–Recent Advances and New Perspectives, IntechOpen London, UK, 2020, pp. 1–23.
- [2] Zhu Jihong, Zhou Han, Wang Chuang, Zhou Lu, Yuan Shangqin, Weihong Zhang, A review of topology optimization for additive manufacturing: Status and challenges, Chin. J. Aeronaut. 34 (1) (2021) 91–110.
- [3] Sourabh Shende, Andrew Gillman, David Yoo, Philip Buskohl, Kumar Vemaganti, Bayesian topology optimization for efficient design of origami folding structures, Struct. Multidiscip. Optim. 63 (2021) 1907–1926.

- [4] Xian Xu, Shaoxiong Huang, Yafeng Wang, Yaozhi Luo, A generalized objective function based on weight coefficient for topology-finding of tensegrity structures, *Appl. Math. Model.* 115 (2023) 541–567.
- [5] M.P. Bendsoe, N. Kikuchi, Generating optimal topologies in structural design using a homogenization method, *Comput. Methods Appl. Mech. Engrg.* 71 (2) (1988) 197–224, [http://dx.doi.org/10.1016/0045-7825\(88\)90086-2](http://dx.doi.org/10.1016/0045-7825(88)90086-2).
- [6] M.P. Bendsoe, O. Sigmund, *Topology Optimization: Theory, Methods, and Applications*, Springer Science & Business Media, 2003.
- [7] X. Huang, M. Xie, *Evolutionary Topology Optimization of Continuum Structures: Methods and Applications*, John Wiley & Sons, 2010.
- [8] G. Allaire, F. Jouve, A.-M. Toader, Structural optimization using sensitivity analysis and a level-set method, *J. Comput. Phys.* 194 (1) (2004) 363–393, <http://dx.doi.org/10.1016/j.jcp.2003.09.032>.
- [9] X. Guo, W. Zhang, W. Zhong, Doing topology optimization explicitly and geometrically—a new moving morphable components based framework, *J. Appl. Mech.* 81 (8) (2014) <http://dx.doi.org/10.1115/1.4027609>.
- [10] T. Buhl, C.B. Pedersen, O. Sigmund, Stiffness design of geometrically nonlinear structures using topology optimization, *Struct. Multidiscip. Optim.* 19 (2) (2000) 93–104, <http://dx.doi.org/10.1007/s001580050089>.
- [11] A. Takezawa, G.H. Yoon, S.H. Jeong, M. Kobashi, M. Kitamura, Structural topology optimization with strength and heat conduction constraints, *Comput. Methods Appl. Mech. Engrg.* 276 (2014) 341–361, <http://dx.doi.org/10.1016/j.cma.2014.04.003>.
- [12] W. Aichtziger, Local stability of trusses in the context of topology optimization part I: exact modelling, *Struct. Optim.* 17 (4) (1999) 235–246.
- [13] G.I. Rozvany, Difficulties in truss topology optimization with stress, local buckling and system stability constraints, *Struct. Optim.* 11 (3) (1996) 213–217, <http://dx.doi.org/10.1007/BF01197036>.
- [14] M. Zhou, Difficulties in truss topology optimization with stress and local buckling constraints, *Struct. Optim.* 11 (2) (1996) 134–136, <http://dx.doi.org/10.1007/BF01376857>.
- [15] X. Xu, Y. Wang, Y. Luo, D. Hu, Topology optimization of tensegrity structures considering buckling constraints, *J. Struct. Eng.* 144 (10) (2018) 04018173, [http://dx.doi.org/10.1061/\(ASCE\)ST.1943-541X.0002156](http://dx.doi.org/10.1061/(ASCE)ST.1943-541X.0002156).
- [16] L. Berke, *An Efficient Approach To the Minimum Weight Design of Deflection Limited Structures*, Rep. Air Force Flight Dynamics Lab, 1970.
- [17] N. Khot, Vb. Venkayya, L. Berke, Optimum structural design with stability constraints, *Internat. J. Numer. Methods Engrg.* 10 (5) (1976) 1097–1114, <http://dx.doi.org/10.1002/nme.1620100510>.
- [18] Y. Wang, X. Xu, Y. Luo, Topology-finding of tensegrity structures considering global stability condition, *J. Struct. Eng.* 146 (12) (2020) 04020260, [http://dx.doi.org/10.1061/\(asce\)st.1943-541x.0002843](http://dx.doi.org/10.1061/(asce)st.1943-541x.0002843).
- [19] M. Neves, H. Rodrigues, J. Guedes, Generalized topology design of structures with a buckling load criterion, *Struct. Optim.* 10 (2) (1995) 71–78, <http://dx.doi.org/10.1007/BF01743533>.
- [20] J. Folgado, H. Rodrigues, Structural optimization with a non-smooth buckling load criterion, *Control Cybernet.* 27 (2) (1998) 235–253.
- [21] X. Gao, H. Ma, Topology optimization of continuum structures under buckling constraints, *Comput. Struct.* 157 (2015) 142–152, <http://dx.doi.org/10.1016/j.compstruc.2015.05.020>.
- [22] X. Gao, L. Li, H. Ma, An adaptive continuation method for topology optimization of continuum structures considering buckling constraints, *Int. J. Appl. Mech.* 9 (07) (2017) 1750092, <http://dx.doi.org/10.1142/S1758825117500922>.
- [23] X. Gao, Y. Li, H. Ma, G. Chen, Improving the overall performance of continuum structures: A topology optimization model considering stiffness, strength and stability, *Comput. Methods Appl. Mech. Engrg.* 359 (2020) 112660, <http://dx.doi.org/10.1016/j.cma.2019.112660>.
- [24] E. Lindgaard, J. Dahl, On compliance and buckling objective functions in topology optimization of snap-through problems, *Struct. Multidiscip. Optim.* 47 (3) (2013) 409–421, <http://dx.doi.org/10.1007/s00158-012-0832-2>.
- [25] P.D. Dunning, E. Ovtchinnikov, J. Scott, H.A. Kim, Level-set topology optimization with many linear buckling constraints using an efficient and robust eigensolver, *Internat. J. Numer. Methods Engrg.* 107 (12) (2016) 1029–1053, <http://dx.doi.org/10.1002/nme.5203>.
- [26] X. Bian, Z. Fang, Large-scale buckling-constrained topology optimization based on assembly-free finite element analysis, *Adv. Mech. Eng.* 9 (9) (2017) 1687814017715422, <http://dx.doi.org/10.1177/1687814017715422>.
- [27] G. Cheng, L. Xu, Two-scale topology design optimization of stiffened or porous plate subject to out-of-plane buckling constraint, *Struct. Multidiscip. Optim.* 54 (5) (2016) 1283–1296, <http://dx.doi.org/10.1007/s00158-016-1542-y>.
- [28] C.R. Thomsen, F. Wang, O. Sigmund, Buckling strength topology optimization of 2D periodic materials based on linearized bifurcation analysis, *Comput. Methods Appl. Mech. Engrg.* 339 (2018) 115–136, <http://dx.doi.org/10.1016/j.cma.2018.04.031>.
- [29] H.-L. Ye, W.-W. Wang, N. Chen, Y.-K. Sui, Plate/shell topological optimization subjected to linear buckling constraints by adopting composite exponential filtering function, *Acta Mech. Sinica* 32 (4) (2016) 649–658, <http://dx.doi.org/10.1007/s10409-015-0531-5>.
- [30] W. Wang, H. Ye, Y. Sui, Lightweight topology optimization with buckling and frequency constraints using the independent continuous mapping method, *Acta Mech. Solida Sin.* 32 (3) (2019) 310–325, <http://dx.doi.org/10.1007/s10338-019-00088-5>.
- [31] Y. Sui, H. Ye, X. Peng, Topological optimization of continuum structure with global stress constraints based on ICM method, in: *Computational Methods*, Springer, 2006, pp. 1003–1014.
- [32] F. Ferrari, O. Sigmund, Revisiting topology optimization with buckling constraints, *Struct. Multidiscip. Optim.* 59 (5) (2019) 1401–1415, <http://dx.doi.org/10.1007/s00158-019-02253-3>.
- [33] F. Ferrari, O. Sigmund, J.K. Guest, Topology optimization with linearized buckling criteria in 250 lines of matlab, *Struct. Multidiscip. Optim.* 63 (6) (2021) 3045–3066, <http://dx.doi.org/10.1007/s00158-021-02854-x>.
- [34] M.K. Singha, L. Ramachandra, J. Bandyopadhyay, Optimum design of laminated composite plates for maximum thermal buckling loads, *J. Compos. Mater.* 34 (23) (2000) 1982–1997, <http://dx.doi.org/10.1177/002199800772661930>.
- [35] P. Malekzadeh, A.R. Vosoughi, M. Sadeghpour, H.R. Vosoughi, Thermal buckling optimization of temperature-dependent laminated composite skew plates, *J. Aerosp. Eng.* 27 (1) (2014) 64–75, [http://dx.doi.org/10.1061/\(ASCE\)AS.1943-5525.0000220](http://dx.doi.org/10.1061/(ASCE)AS.1943-5525.0000220).

- [36] S. Kamarian, M. Shakeri, M.H. Yas, Thermal buckling optimisation of composite plates using firefly algorithm, *J. Exp. Theor. Artif. Intell.* 29 (4) (2017) 787–794, <http://dx.doi.org/10.1080/0952813X.2016.1259267>.
- [37] S. Deng, K. Suresh, Topology optimization under thermo-elastic buckling, *Struct. Multidiscip. Optim.* 55 (5) (2017) 1759–1772, <http://dx.doi.org/10.1007/s00158-016-1611-2>.
- [38] B. Stanford, P. Beran, Aerothermoelastic topology optimization with flutter and buckling metrics, *Struct. Multidiscip. Optim.* 48 (1) (2013) 149–171, <http://dx.doi.org/10.1007/s00158-013-0885-x>.
- [39] C. Wu, J. Fang, Q. Li, Multi-material topology optimization for thermal buckling criteria, *Comput. Methods Appl. Mech. Engrg.* 346 (2019) 1136–1155, <http://dx.doi.org/10.1016/j.cma.2018.08.015>.
- [40] M. Stolpe, K. Svanberg, An alternative interpolation scheme for minimum compliance topology optimization, *Struct. Multidiscip. Optim.* 22 (2) (2001) 116–124, <http://dx.doi.org/10.1007/s001580100129>.
- [41] N. Gan, Q. Wang, Topology optimization design for thermal buckling criterion with the size effect, *Mech. Based Des. Struct. Mach.* (2021) 1–18, <http://dx.doi.org/10.1080/15397734.2021.1981378>.
- [42] N. Gan, Q. Wang, Topology optimization design of porous infill structure with thermo-mechanical buckling criteria, *International Journal of Mechanics and Materials in Design* 18 (2) (2022) 267–288, <http://dx.doi.org/10.1007/s10999-021-09575-5>.
- [43] H.M. Lee, K.K. Lee, G.H. Yoon, Topography and size optimization of composite structure to control buckling temperature and thermal buckling mode shape, *Thin-Walled Struct.* 171 (2022) 108686, <http://dx.doi.org/10.1016/j.tws.2021.108686>.
- [44] O. Sigmund, Design of multiphysics actuators using topology optimization—part I: One-material structures, *Comput. Methods Appl. Mech. Engrg.* 190 (49–50) (2001) 6577–6604, [http://dx.doi.org/10.1016/S0045-7825\(01\)00251-1](http://dx.doi.org/10.1016/S0045-7825(01)00251-1).
- [45] O. Sigmund, Design of multiphysics actuators using topology optimization—part II: Two-material structures, *Comput. Methods Appl. Mech. Engrg.* 190 (49–50) (2001) 6605–6627, [http://dx.doi.org/10.1016/S0045-7825\(01\)00252-3](http://dx.doi.org/10.1016/S0045-7825(01)00252-3).
- [46] P.D.L. Jensen, F. Wang, I. Dimino, O. Sigmund, Topology optimization of large-scale 3D morphing wing structures, *Actuators* 10 (9) (2021) 217, <http://dx.doi.org/10.3390/act10090217>.
- [47] R.D. Cook, et al., *Concepts and Applications of Finite Element Analysis*, John Wiley & sons, 2007.
- [48] F. Wang, B.S. Lazarov, O. Sigmund, On projection methods, convergence and robust formulations in topology optimization, *Struct. Multidiscip. Optim.* 43 (6) (2011) 767–784, <http://dx.doi.org/10.1007/s00158-010-0602-y>.
- [49] O.C. Zienkiewicz, R.L. Taylor, *The Finite Element Method for Solid and Structural Mechanics*, Elsevier, 2005.
- [50] R. De Borst, M.A. Crisfield, J.J. Remmers, C.V. Verhoosel, *Nonlinear Finite Element Analysis of Solids and Structures*, John Wiley & Sons, 2012.
- [51] W. Zhang, J. Yang, Y. Xu, T. Gao, Topology optimization of thermoelastic structures: mean compliance minimization or elastic strain energy minimization, *Struct. Multidiscip. Optim.* 49 (3) (2014) 417–429, <http://dx.doi.org/10.1007/s00158-013-0991-9>.
- [52] G. Kreisselmeier, R. Steinhauser, Systematic control design by optimizing a vector performance index, in: *Computer Aided Design of Control Systems*, Elsevier, 1980, pp. 113–117.
- [53] M. Bruyneel, P. Duysinx, Note on topology optimization of continuum structures including self-weight, *Struct. Multidiscip. Optim.* 29 (4) (2005) 245–256, <http://dx.doi.org/10.1007/s00158-004-0484-y>.
- [54] T. Gao, W. Zhang, Topology optimization involving thermo-elastic stress loads, *Struct. Multidiscip. Optim.* 42 (5) (2010) 725–738, <http://dx.doi.org/10.1007/s00158-010-0527-5>.
- [55] J. Zhu, W. Zhang, Integrated layout design of supports and structures, *Comput. Methods Appl. Mech. Engrg.* 199 (9–12) (2010) 557–569, <http://dx.doi.org/10.1016/j.cma.2009.10.011>.
- [56] S. Cho, J.-Y. Choi, Efficient topology optimization of thermo-elasticity problems using coupled field adjoint sensitivity analysis method, *Finite Elem. Anal. Des.* 41 (15) (2005) 1481–1495, <http://dx.doi.org/10.1016/j.finel.2005.05.003>.
- [57] K. Svanberg, The method of moving asymptotes—a new method for structural optimization, *Internat. J. Numer. Methods Engrg.* 24 (2) (1987) 359–373, <http://dx.doi.org/10.1002/nme.1620240207>.
- [58] V.F. Demyanov, V.N. Malozemov, *Introduction To Minimax*, Courier Corporation, 1990.
- [59] H. Aissi, C. Bazgan, D. Vanderpooten, Min–max and min–max regret versions of combinatorial optimization problems: A survey, *European J. Oper. Res.* 197 (2) (2009) 427–438, <http://dx.doi.org/10.1016/j.ejor.2008.09.012>.
- [60] M.A. Wadee, N. Hadjipantelis, J.B. Bazzano, L. Gardner, J.A. Lozano-Galant, Stability of steel struts with externally anchored prestressed cables, *J. Construct. Steel Res.* 164 (2020) 105790, <http://dx.doi.org/10.1016/j.jcsr.2019.105790>.